Three-Dimensional Kinematic and Microphysical Evolution of Florida Cumulonimbus. Part II: Frequency Distributions of Vertical Velocity, Reflectivity, and Differential Reflectivity

SANDRA E. YUTER AND ROBERT A. HOUZE JR.

Department of Atmospheric Sciences, University of Washington, Seattle, Washington

(Manuscript received 31 March 1994, in final form 30 November 1994)

ABSTRACT

High-resolution radar data collected in Florida during the Convection and Precipitation/Electrification Experiment are used to elucidate the microphysical and kinematic processes occurring during the transition of a multicellular storm from convective to stratiform stages. A statistical technique is employed to examine the evolving properties of the ensemble small-scale variability of radar reflectivity, vertical velocity, and differential reflectivity over the entire storm.

Differential radar reflectivity data indicate that the precipitation at upper levels was nearly glaciated early in the storm's lifetime. Dual-Doppler radar data show that throughout the storm's lifetime both updrafts and downdrafts were present at all altitudes and that most of the volume of the radar echo contained vertical velocities incapable of supporting precipitation-size particles. Thus, the ensemble microphysical properties of the storm were increasingly dominated by particles falling in an environment of weak vertical velocity, and the radar reflectivity began to take on a statistically stratiform character during the early stages of the storm. This stratiform structure became more distinct as the storm aged.

Two dynamically distinct downdrafts were indicated. Lower-level downdrafts were associated with precipitation. Upper-level downdrafts were dynamically associated with the stronger upper-level updrafts and were likely primarily a consequence of the pressure gradient forces required to maintain mass continuity in the presence of buoyant updrafts.

1. Introduction

Yuter and Houze (1995a), henceforth referred to as YH Part I, use spatial cross sections to characterize a line of thunderstorms near the east coast of Florida. In this second part of the study, we examine statistically the changes in the distribution of vertical velocity, reflectivity, and differential reflectivity as the storm evolves.

Previous studies (Houze 1989; Biggerstaff and Houze 1991, 1993; Mapes and Houze 1993) have documented the gross vertical air motion and radar reflectivity characteristics of convective and stratiform regions derived from Doppler radar and composite sounding analyses around the world. The shapes of the mean vertical profiles of vertical velocity and radar reflectivity in convective and stratiform regions are roughly consistent across storms in different regimes (tropical oceanic, tropical continental, midlatitude continental, etc.). Variations in magnitude among these profiles are a result of differences in regime and differences in the space and time resolution of the mea-

surements analyzed to obtain the profiles. Characteristic mean vertical profiles of vertical velocity and radar reflectivity from a case from PRE-STORM[1] are illustrated in Fig. 1. Profiles of mean vertical velocity in convection (Fig. 1a, solid line) increase from a low value at low levels to a peak value at middle to upper levels, and then decrease in value toward the top of the storm. In stratiform regions (Fig. 1a, dotted line), the mean vertical velocity profile resembles a sine curve along the vertical. Near the surface, the mean vertical velocity is close to zero. It then decreases at low levels so that the region below the environmental 0°C level is dominated by weak downdrafts. Above the vicinity of the 0°C level, the profile of mean vertical velocity in stratiform regions increases and crosses over zero. Weak updrafts dominate at mid- and upper levels. The mean value decreases, finishing off the sine curve with a value approaching zero near the top of the storm. The characteristic mean profile of radar reflectivity in convective regions (Fig. 1b, solid line) exhibits a relatively constant reflectivity from the surface to several kilo-

---

Corresponding author address: Sandra E. Yuter, Department of Atmospheric Sciences, University of Washington, Box 351640, Seattle, WA 98195.
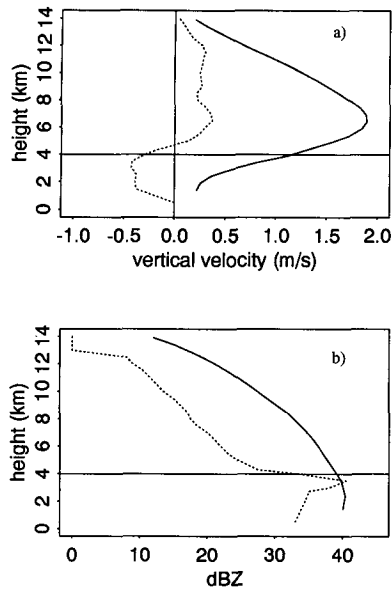
FIG. 1. Characteristic mean profiles in convective (solid lines) and stratiform (dashed lines) regions in the 10–11 June 1985 mesoscale convective system observed in Kansas during the PRE-STORM project. (a) Vertical velocity and (b) mean reflectivity. The horizontal line at 4 km indicates the 0°C level. Profiles provided by S. Braun.

meters above the environmental 0°C level. At higher levels, the mean reflectivity within convective regions decreases gradually toward storm top. Within stratiform regions, the mean radar reflectivity (Fig. 1b, dotted line) has a sharp maximum just below the environmental 0°C level. The value of the mean reflectivity profile then decreases sharply within the first few kilometers above the level of the maximum value and then decreases more gradually at higher levels.

The typical mean profiles (Fig. 1) characterize two different states of the storm. To understand better how a group of convective cells in a cumulonimbus complex evolves from a highly convective state to a more stratiform state, we examine the evolution of the small-scale variability of the Convection and Precipitation/Electrification Experiment (CaPE) storm of 15 August 1991.

The high-resolution radar data obtained in CaPE thunderstorms revealed a detailed and complex pattern of cells, updrafts, and downdrafts (YH Part I). No single horizontal or vertical cross section of the data is representative of the radar echo pattern. This problem motivated us to display the data in a statistical manner. We examine the frequency distributions of reflectivity Z, vertical velocity w, and differential reflectivity Z_{DR} as functions of height at a series of times. This procedure allows the ensemble properties of updrafts, downdrafts, and reflectivity features to be investigated, and it elucidates the evolution of the collection of cells from a highly convective state to a nearly stratiform state. The details of the evolution from convective to stratiform states have been nearly impossible to determine

from previous lower-resolution datasets and cross-section-based methodologies; their revelation was the main purpose of this study.

2. Statistical methodology—Contoured frequency by altitude diagrams

a. Description

The diagrams used to display the statistical distributions of the storm properties are henceforth referred to as contoured frequency by altitude diagrams (CFADs). The ordinate of the CFAD is height, and the abscissa is the value of the parameter whose distribution is being plotted. Contours of frequency of the parameter value are then plotted in this coordinate system. An additional contribution of this study is the demonstration of the utility of the CFADs in revealing aspects of storm structure not easily gleaned from examination of conventional spatial cross sections.

Averages can be used to estimate the behavior of a "typical" individual element of the ensemble when a distribution is known and unimodal. The frequency distributions of radar-derived parameters such as reflectivity and vertical velocity are typically non-Gaussian and often multimodal. The CFAD preserves the information in the frequency distribution.

The CFAD also overcomes the mismatch in space scales and timescales of radar data. The time between scans (with present technology) is typically not commensurate with the high spatial resolution of the radar data. Individual updrafts, downdrafts, and reflectivity cores cannot be followed unambiguously from one scan to the next. However, the ensemble properties of the whole sample of cells vary more slowly. Therefore, the CFADs allow us to examine the convective life cycle by examining changes in ensemble properties from one radar scan to the next instead of following individual convective entities from one time to the next.

A further motivation for a robust methodology for readily identifying the essential properties of a large volume of radar data is that the interpretation of radar data has some inherent ambiguities. Data must often be hand edited to unfold regions of radial velocity data into their correct Nyquist intervals (Rinehart 1991, p. 81) and to remove apparently spurious data such as second-trip echoes (Rinehart 1991, p. 83) and flare echoes (Wilson and Reum 1988). In any given volume, the value of the radial velocity at a few points is ambiguous. Leaving, correcting, or deleting these few points will affect the synthesized Doppler velocity fields in some way. The reflectivity data at some points are also subject to ambiguities as a result of attenuation, beam geometry, and other factors. We sought a method for visualizing the data that would not be sensitive to the interpretation of the radar data at a single point in the volume. The statistical presentation of the CFAD is a more robust display of information in an entire

radar echo volume than the arbitrary subset of data presented in a cross section.

b. Definition

The CFAD[2] summarizes frequency distribution information about a variable A in a given radar echo volume in a single contour plot.[3] To obtain this plot, the data are stratified by altitude only, and the horizontal locations of the data are ignored. The frequency of occurrence of A at a given height is retained.

Figure 2a shows the frequency distribution of reflectivity values from the 8-km level of the 2139 UTC dual-Doppler volume (Fig. 8b of YH Part I). Similar histograms are computed for each altitude in the volume. The single-level histograms for each altitude are normalized to the number of data points at each level and then arranged in sequence along the height axis (Fig. 2b). The histogram for the 8-km level (Fig. 2a) is highlighted in Fig. 2b. The surface shown in Fig. 2b summarizes the characteristics of the histograms for all levels in the storm and thus characterizes the ensemble properties of the storm. The topography of this surface changes as the storm evolves. We use these changes in the topography of the frequency distribution to study storm evolution.

To simplify presentation, we replace the perspective view in Fig. 2b with a contoured topographic map similar to that produced from elevation data for a mountain (Fig. 2c). The data for the 8-km level (Fig. 2a) is highlighted by the dotted line in Fig. 2c. The topographic map is the CFAD. Any volume of radar data can be represented as a CFAD. With one figure, the CFAD communicates information about the width of the frequency distribution at each level and the number, values, skewness, and degree of peakedness (kurtosis) of the frequency distribution modes for the entire storm volume.

CFADs of reflectivity and vertical velocity were constructed for each of the five dual-Doppler volumes (Fig. 3) to show the evolving topography of the frequency distributions of reflectivity and vertical velocity in the storm under study here. The CFAD shown in Fig. 2c is Fig. 3c. CFADs of Z_{DR} were constructed from the three volumes of CP-2 data (section 4). All these plots were constructed for the echo volume within the stationary 40 km $\times$ 39 km $\times$ 17.2 km radar volume grid described in YH Part I, section 4. Only those points in the volume where $Z > -15$ dBZ and where vertical velocity could be deduced from the Doppler measure-

ments were used in construction of the CFADs.[4] This procedure eliminated areas of low reflectivity at low levels, where the radar echo was of insufficient vertical extent to obtain a reliable vertical velocity estimate. Since each volume contains many convective cells at different stages of their life cycles, the CFADs show how the ensemble properties of the group of cells evolve.

The contours in the CFADs do not represent the percentage of data points but rather the percentage of points per unit variable per kilometer. The particular contour intervals used for each of the CFADs are indicated in their accompanying figure captions. (The numerical values of the contours are an artifact of the histogram bin widths. See appendix A for further details.) The values of contours used in the CFADs were chosen to show the shape of the topography of the distribution. The spatial pattern of the CFAD contours reveals the steepness (closely packed contours) or flatness (widely spaced contours) of the frequency distribution topography. By comparing the pattern of contours, the relative concentration of the frequency distribution between levels in the same volume and between the same level at different times can be compared.

c. Percentage cumulative area coverage plots

The cumulative echo area containing vertical velocities less than a given vertical velocity threshold at a given altitude is expressed as a percentage of total echo covered area at that height and is plotted in Fig. 4 for several vertical velocity thresholds (-10, -5, -2, 0, 2, 5, and 10 m s^{-1}). These plots were constructed from the same volumes of vertical velocity data used in the CFADs (Fig. 3). They complement the CFADs by quantifying the relative proportions of echo area occupied by various vertical velocities and how these proportions change with height. For example, the curve for the zero vertical velocity threshold at 2155 UTC (Fig. 4c) shows that the amount of area covered by upward-moving air increases with height from 40% at 1 km to 60% at upper levels.

3. Reflectivity and vertical velocity

Figure 3 shows CFADs of both radar reflectivity Z and vertical velocity w for five volume time periods during the evolution of the 15 August 1991 line of thunderstorms (Table 2 of YH Part I). At the last time shown (2237 UTC), the storm was in transition toward a stratiform state. After 2237 UTC, the storm was out-

---

[2] A mathematical description of the CFAD is given in appendix A.

[3] Black et al. (1991) used a variation of the contoured frequency by altitude diagrams described here to examine the frequency distribution of a two-dimensional dataset of vertical velocities from vertical incidence airborne radar data.

---

[4] For convenience, these points within the 40 km $\times$ 39 km $\times$ 17.2 km Cartesian grid will be termed the *radar echo volume* or *echo volume*.
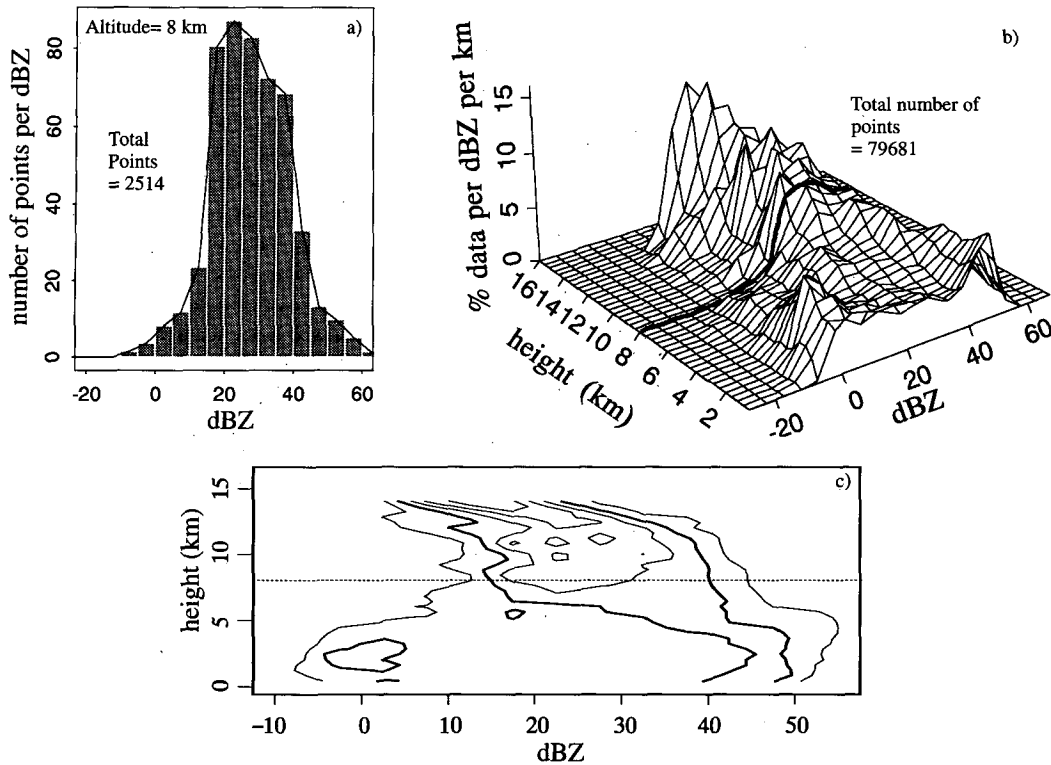
FIG. 2. (a) Single-level histogram of radar reflectivity at 8 km for 2139 UTC. Histogram bin width is 5 dBZ. (b) Perspective view of frequency by altitude diagram of radar reflectivity for 2139 UTC volume. Heavy line corresponds to single-level histogram at 8 km shown in (a). (c) The 2139 UTC reflectivity CFAD. The bin size is 5 dBZ, and the plot is contoured at intervals of 2.5% of data per dBZ per kilometer with the 5% dBZ^{-1} km^{-1} contour highlighted. Horizontal dashed line at 8 km corresponds to data contained in the single-level histogram in (a). The CFAD in (c) is truncated above 14.8 km where the number of available data points were considered too few to be representative of the storm structure. See appendix A for further details.

side the dual-Doppler area. Trends in the evolution of the CFADs in Fig. 3 are described below.

a. Dominance of weakly upward- and downward-moving air and implications for precipitation processes

An irregular ridge centered near 0 m s^{-1} dominates each of the CFADs of vertical velocity (Figs. 3b,d,f,h,j). Both updrafts and downdrafts were present at all altitudes at all times. The distribution of vertical velocity in the CFADs indicates that the most common values of vertical velocity were low (-1.5 m s^{-1} $< w$ < 2.5 m s^{-1}). The weak vertical velocities were contributed by a combination of weak drafts and regions of weak vertical velocities on the periphery of drafts with stronger peak magnitudes (Figs. 7–9 of YH Part I). Vertical velocities greater than 5 m s^{-1} were infrequent, and values exceeding 10 m s^{-1} were even less frequent (Figs. 3 and 4). This fact has important cloud microphysical implications since the precipitation particles in the storm volume were most frequently falling

in the presence of weak vertical velocities, even when the storm was in a very active convective stage.

An updraft velocity of close to 2 m s^{-1} is needed to support most snow particles (Locatelli and Hobbs 1974). Thus, it is likely that most of the growth of glaciated precipitation particles that were rising in the storm was occurring in updrafts in the range 2 m s^{-1} $< w < 5$ m s^{-1} since regions with $w > 5$ m s^{-1} comprised a smaller fraction of storm volume (Figs. 3 and 4). At these moderate vertical velocities, sufficient vapor and liquid water are available for depositional and/or accretional growth of the precipitation particles. Although supersaturation and condensation rates generally increase with increasing vertical velocity, the longer time a parcel takes to reach a given altitude in a weak updraft approximately compensates for the higher supersaturations present in stronger updrafts (Rogers and Yau 1989). Once cloud water is available, particle growth to precipitation size can occur by deposition and/or accretion in updrafts that are strong enough to suspend the particles (Pruppacher and Klett 1978; Braun and Houze 1994). In drafts where $w < 2$ m s^{-1}, which occupy the majority of the volume even
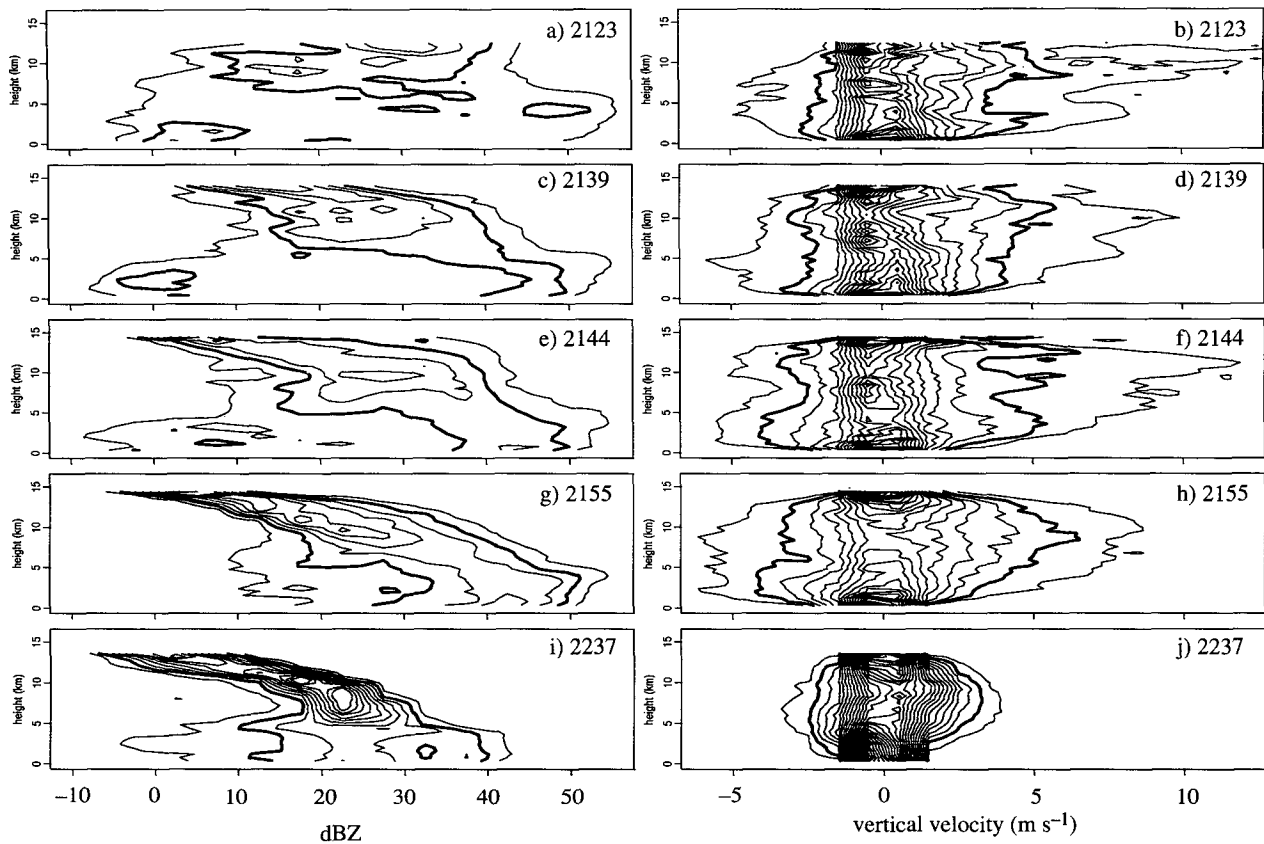
FIG. 3. Time series of CFADs of radar reflectivity (left) and vertical velocity frequency (right): (a) 2123 UTC Z, (b) 2123 UTC w, (c) 2139 UTC Z, (d) 2139 UTC w, (e) 2144 UTC Z, (f) 2144 UTC w, (g) 2155 UTC Z, (h) 2155 UTC w, (i) 2237 UTC Z, (j) 2237 UTC w. For reflectivity CFADs the bin size is 5 dBZ and the plot is contoured at intervals of 2.5% of data per dBZ per kilometer with the 5% dBZ^{-1} km^{-1} contour highlighted. In the vertical velocity CFADs, the bin size is 1 m s^{-1}, and the plot is contoured at intervals of 5% of data per meter per second per kilometer with the 10% m^{-1} s km^{-1} contour highlighted.

during the highly convective stages of the storm (Fig. 4) and in which precipitation particles must be falling, the growth of precipitation particles must occur primarily by deposition, aggregation, and riming.

b. Diagonalization of the reflectivity CFADs

In the early stages of the storm (Figs. 3a,c), the distribution of reflectivity was wide at all altitudes and multimodal at several altitudes. As the storm became more vigorous and mature (Figs. 3e,g,i), the CFADs show a distinctive narrowing of the frequency distribution topography of reflectivity, particularly above the 0°C level (4.4 km), into a sharp unimodal diagonal ridge of increasing reflectivity with decreasing height.

The origin of the wide distribution and modes of reflectivity in the earliest stage of the storm can be investigated with the aid of vertical profiles of the updraft and downdraft components of mean reflectivity and vertical velocity (Figs. 5a and 6a) and the highest frequency mode of reflectivities (Fig. 7). Different features of the CFAD of reflectivity at 2123 (Fig. 3a) are

associated with upward- and downward-moving air. The weak peak in the frequency distribution of reflectivity at low levels between −1 and 12 dBZ (indicated by the 5% dBZ^{-1} km^{-1} contour in Fig. 3a) is associated with updrafts (Fig. 7a) and thus appears to have been related to weak radar echoes produced by convergence in the boundary layer. Below 5 km, both the mean and mode reflectivity within downdrafts were higher than within updrafts (Figs. 5a and 7), implying that the downdrafts at lower levels were associated with heavier precipitation. In contrast, above 6 km the higher reflectivity values tended to be associated with the updrafts, as evidenced by the mean and mode reflectivity within updrafts being higher than within downdrafts (Figs. 5a and 7). The mode of the frequency distribution of reflectivity within downdrafts (Fig. 7b) was near 15 dBZ at mid- and upper levels. Evidently, the upper-level downdrafts were not driven by precipitation drag.

During the increasingly energetic convective stage of the storm (2139 UTC) at levels above 10 km, the CFAD of reflectivity displays the beginning of a trend toward narrowing into a unimodal diagonal zone in the
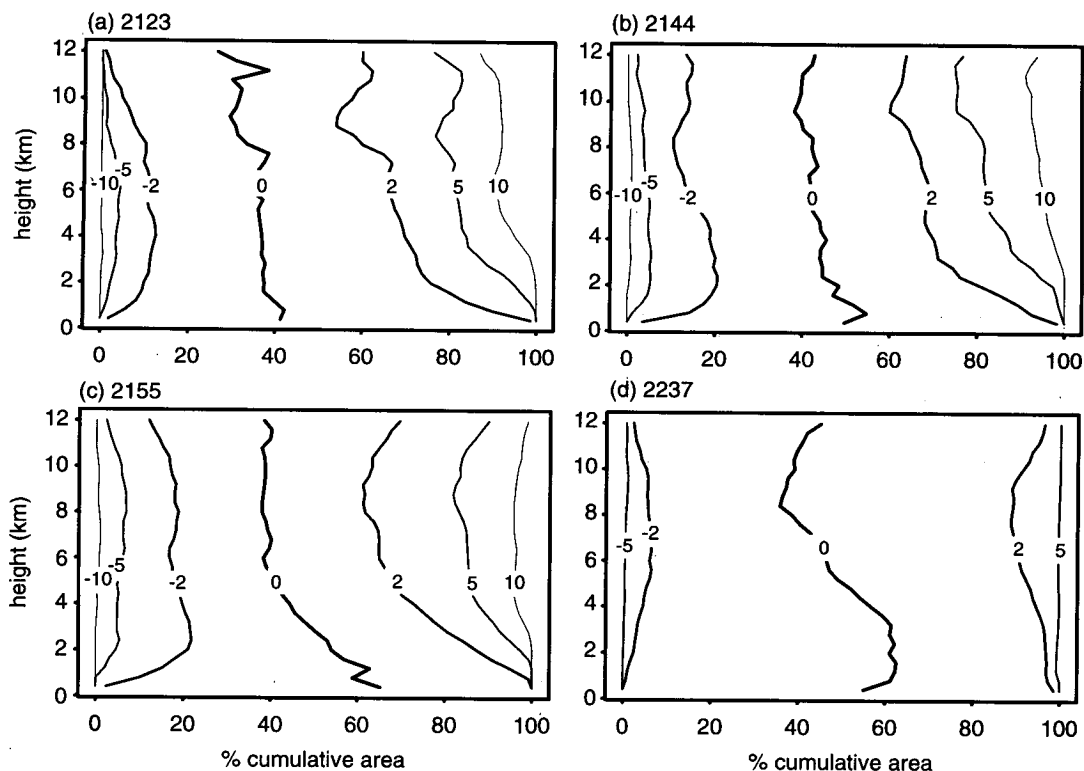
FIG. 4. Time series of plots summarizing cumulative area coverage of vertical velocity at each level as a function of height. Each curve shows the percentage of radar echo area at a given altitude containing vertical velocities less than the indicated threshold value (-10, -5, -2, 0, 2, 5, 10 m s^{-1}). At 2237 UTC, vertical velocities within the echo volume had absolute values less than 10 m s^{-1}. Different line weights were used to enhance readability.

frequency distribution topography (indicated by the 5% dBZ^{-1} km^{-1} contour in Fig. 3c). Further concentration into this diagonal is seen at subsequent times (Figs. 3e,g,i). The narrowing diagonal signals an increasingly uniform reflectivity at a given height and an increase of reflectivity downward. The wide, multimodal spectrum of reflectivities seen at high levels in Fig. 3a thus quickly began to sharpen as the precipitation evolved from an early convective state toward maturity (Fig. 3g). Evidently, as the storm matured, fewer new particles associated with higher reflectivity were injected into upper levels, and the larger, denser, and more reflective ice particles that were present earlier fell out.[5]

The horizontal cross section at the 8-km altitude shows that the radar echo along the north–south line

was more continuous at 2139 (Fig. 8b of YH Part I) than it had been at 2123 (Fig. 9a of YH Part I). The falling particles between the stronger updrafts probably aided in the consolidation of the reflectivity echo of the line of cells.

At low levels, another trend was becoming evident at 2139 UTC. The low-level peak in the frequency distribution of reflectivity (Fig. 3c) near 0 dBZ (5% dBZ^{-1} km^{-1} contour) was beginning to weaken. Reflectivity values less than 10 dBZ would essentially disappear by 2155 UTC (Fig. 3g). Concurrently, the frequency of values between 40 and 50 dBZ was increasing (5% dBZ^{-1} km^{-1} contour in Figs. 3c,e,g,i). The increasing frequency of points at these high reflectivity values near the surface indicates that larger areas of the storm were raining at rates[6] greater than 20 mm h^{-1}. The small-scale horizontal variability of this rain rate is illustrated by the rain gauge readings (Fig. 6 of YH Part I).

---

[5] The more reflective, heavier ice particles associated with $Z > 40$ dBZ, which disappear from the frequency distributions from altitudes greater than 10 km (Figs. 3c,e,g), would have had an approximate fall speed of 2–3 m s^{-1} if they were composed of snow (Marks and Houze 1987). If these higher reflectivity particles were graupel, they could have had higher fall speeds (Locatelli and Hobbs 1974). The 32 min between 2123 and 2155 UTC would be sufficient time for these more reflective particles to fall out of upper levels of the storm.

[6] The GATE Z–R relation [$Z = 230R^{1.25}$ (Austin et al. 1976; Hudlow 1979)] is used to approximate rain rate R from Z values. GATE is the abbreviation for GARP (Global Atmospheric Research Program) Atlantic Tropical Experiment (Houze and Betts 1981).
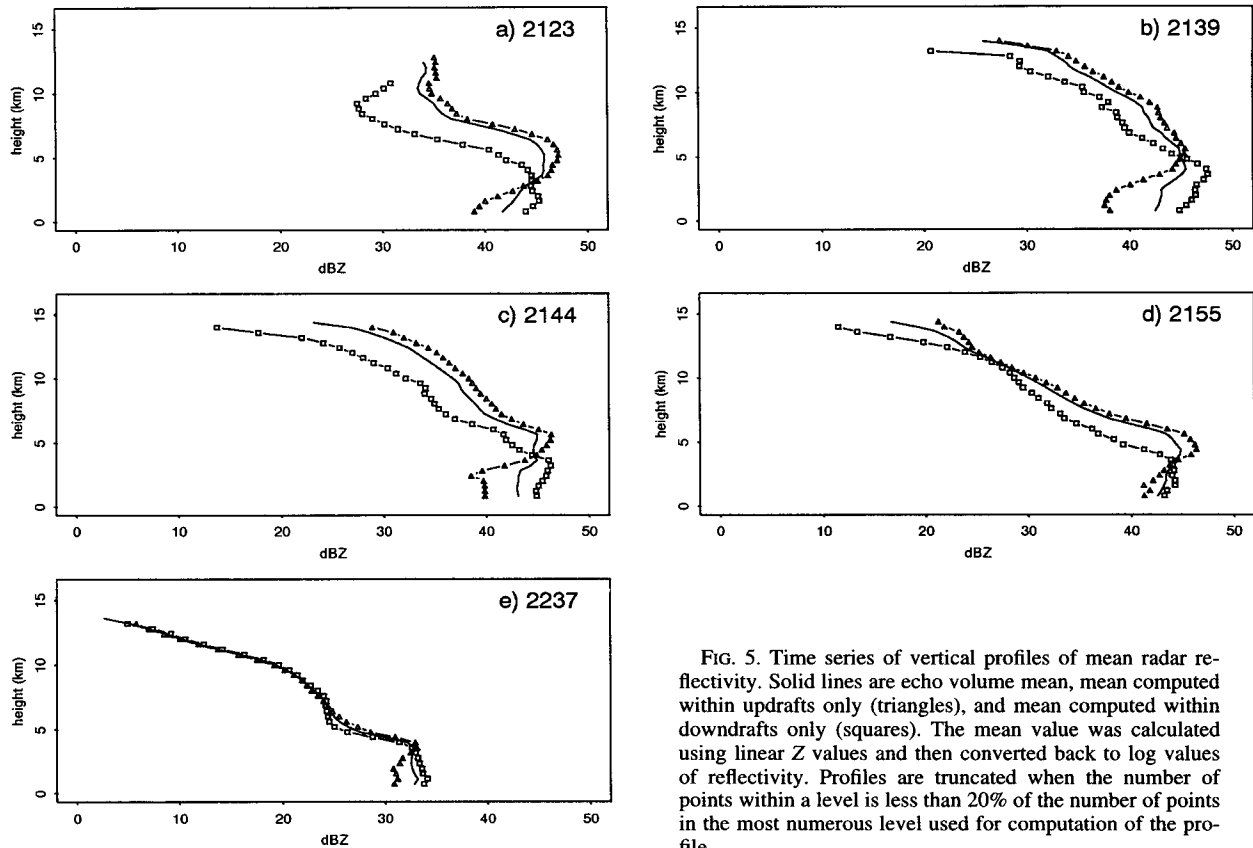
FIG. 5. Time series of vertical profiles of mean radar reflectivity. Solid lines are echo volume mean, mean computed within updrafts only (triangles), and mean computed within downdrafts only (squares). The mean value was calculated using linear Z values and then converted back to log values of reflectivity. Profiles are truncated when the number of points within a level is less than 20% of the number of points in the most numerous level used for computation of the profile.

As the storm began to fade (2237 UTC), the spatial pattern of radar reflectivity lost its previous cellular character, and the reflectivity became weaker and more homogenous (Figs. 8e and 9e of YH Part I). The storm was in a transitional stage (YH Part I, section 2) in which the vertical velocities associated with the decaying convection were still strong enough that the storm was not yet truly stratiform. Convective-scale updrafts and downdrafts, probably remnants of previously stronger drafts, were still found throughout the radar echo volume but were considerably weaker than earlier (Fig. 3j). Mean reflectivity values (Fig. 5e) were lower at all levels compared to those at previous times. The tightly spaced contours in the CFAD of reflectivity (Fig. 3i) from 5 km upward indicate that the horizontal uniformity of reflectivity had increased considerably compared to the 2155 UTC volume. The slope in reflectivity with decreasing height along the diagonal[7] is

approximately 4 dB km^{-1}. This structure in the CFAD at 2237 is consistent with ice particles growing, aggregating, and melting during their descent. The dominant regime at mid- and upper levels appears to have been one of falling ice; that is, when viewed in the statistical perspective provided by the CFAD, the reflectivities at this transitional stage of the storm's evolution exhibited a stratiform-like structure even though technically the volume does not qualify as stratiform (as defined in section 2 of YH Part I).

To compare the convective and transitional structures seen in Fig. 3 to a storm in a more highly developed stratiform state, Fig. 8 shows CFADs of reflectivity and vertical velocity for the stratiform region of the

---

[7] This increase in reflectivity with decreasing height reflects the mode of the distribution for the entire storm. Several authors have computed the vertical profile of maximum radar reflectivity for storm cell cores in a variety of environments (Donaldson 1961; Konrad 1978; Szoke et al. 1986; Jorgensen and LeMone 1989; Zipser and

Lutz 1994). The profiles presented in this paper are not strictly comparable to their profiles. The Z profiles for the entire storm presented here, and those for storm cores, nonetheless have the same basic characteristic of Z decreasing in height above the 0°C level. The 4 dB km^{-1} slope of our profiles above the 0°C level for the entire storm volume is close to the slope of 3.5 dB km^{-1} observed in storm cores in continental tropical convection in Australia (Zipser and Lutz 1994). Core reflectivity profiles tend to exhibit higher slopes as overall reflectivity weakens (Konrad 1978). Our distributions show a similar trend, with slope increasing slightly as the storm matures and weakens.
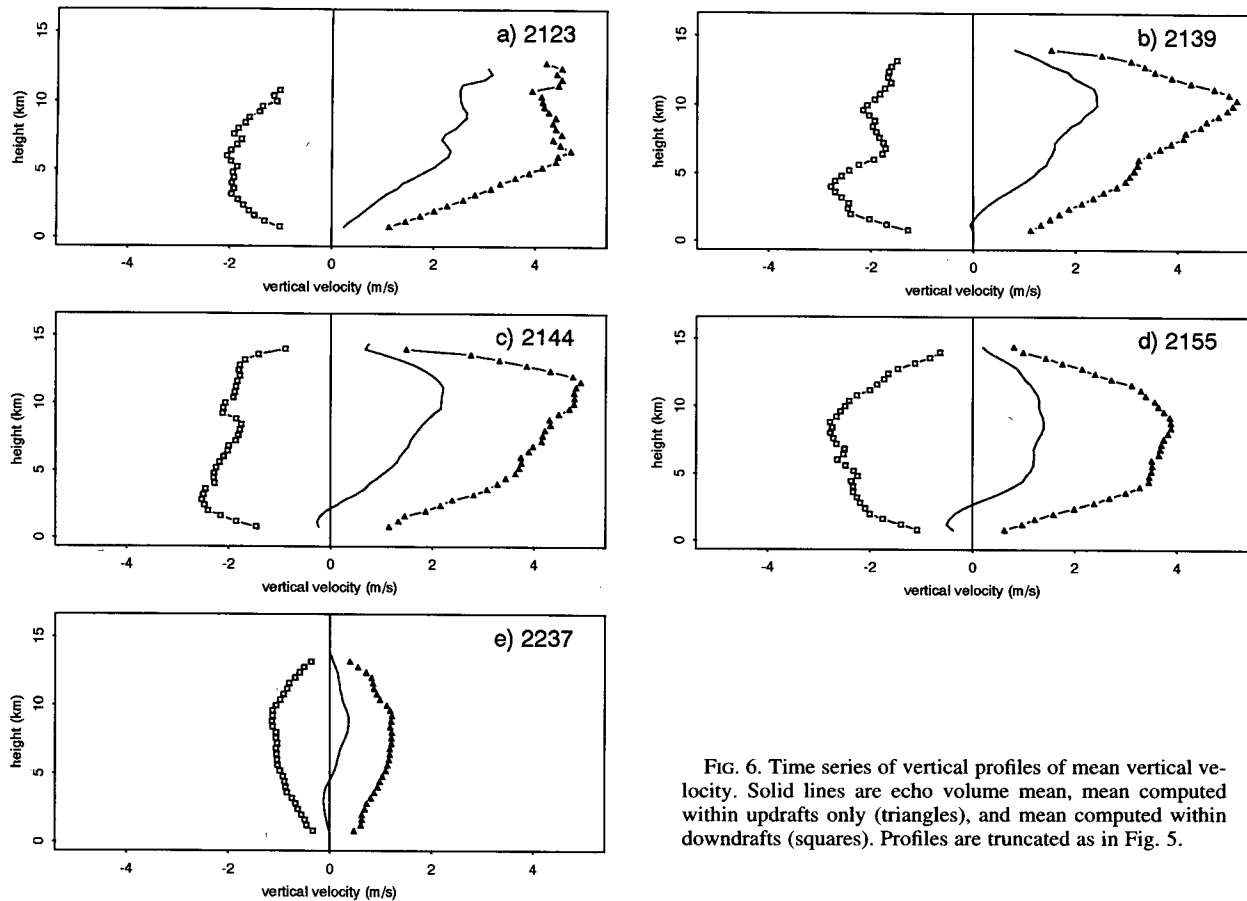
FIG. 6. Time series of vertical profiles of mean vertical velocity. Solid lines are echo volume mean, mean computed within updrafts only (triangles), and mean computed within downdrafts (squares). Profiles are truncated as in Fig. 5.

extensively studied PRE-STORM case of 10–11 June 1985 (Rutledge et al. 1988; Biggerstaff and Houze 1991).[8] The CFAD of reflectivity (Fig. 8a) for the PRE-STORM stratiform region illustrates the continuation of the diagonalization trend seen in the convective and transitional stages of the storm in the CaPE volumes. The stratiform reflectivity CFAD shows an extremely tight frequency distribution, within ±5 dBZ from the mode value, representing a nearly homogenous field of reflectivity at each level (Fig. 8a). The diagonal trend in the frequency distribution of reflectivity continues down until near 5 km. Just below this level, there is a strong enhancement of reflectivity associated with melting in the radar bright band. The

maximum in reflectivity occurs near the 0°C level[9] at about 4 km. Below 4 km, reflectivity decreases as the larger wet ice particles collapse into smaller drops, and the fall speeds of the particles increase, thereby reducing the rainwater concentration in the radar resolution volume (Houze 1993, chapter 6).

During the convective and transitional stages of the storm, the maximum value of reflectivity in the frequency distribution, represented by the 2.5% dBZ^{-1} km^{-1} contour, increases rapidly with decreasing height from near 7 to 5 km and peaks near 4–5 km (Figs. 3a,c,e,g,i). The altitude of the maximum of reflectivity occurs near the 0°C level (4.4 km), where the change of phase of precipitation particles produces a radar reflectivity bright band in vertical cross sections within stratiform precipitation. However, for these volumes no radar bright band was evident in individual vertical cross sections. Physical interpretation of the

---

[8] In order to obtain a purely stratiform volume, a stratiform subarea from one dual-Doppler volume was extracted. The stratiform subarea was selected subjectively from the 0345 UTC 11 June 1985 dual-Doppler volume centered in the PRE-STORM eastern dual-Doppler lobe. The stratiform volume was 9295 km^2 in horizontal area. Grid size in the stratiform volume was 1.5 km in the horizontal and 0.5 km in the vertical.

[9] The sounding through this stratiform region had a 0°C isothermal layer between 3.8 and 4.1 km (Rutledge et al. 1988).
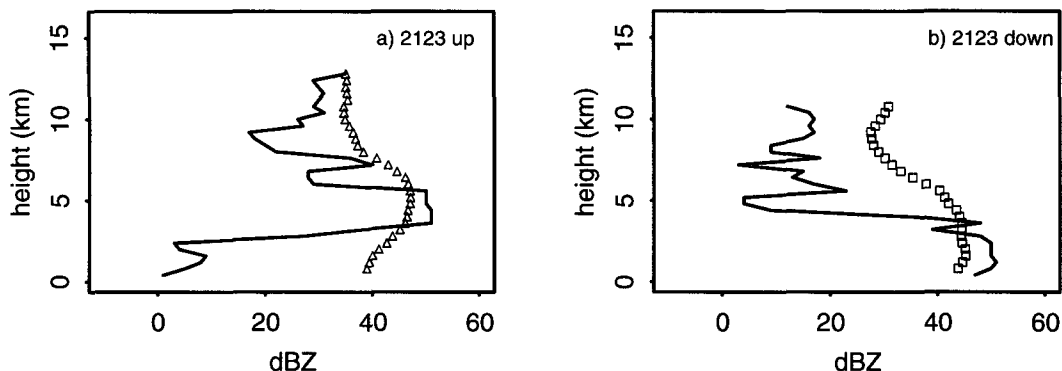
FIG. 7. Comparison of mean and mode of radar reflectivity at 2123 UTC within upward- and downward-moving air. (a) Within updrafts—mode solid line, mean—triangles; (b) within downdrafts, mode—solid line, mean—squares. Profiles are truncated as in Fig. 5.

reflectivity maximum near the 0°C level within a highly convective storm volume is aided by interpretation of the Z_{DR} observations (section 4).

c. Changing vertical distribution of updrafts and downdrafts

The frequency distributions of vertical velocity (Figs. 3b,d,f,h,j) developed several characteristics as the storm evolved. At the first three times in Fig. 3 (2123, 2139, and 2144 UTC), the changes in the frequency distribution of vertical velocity were most evident in the outliers of the distribution (5% and 10% m^{-1} s km^{-1} contours). Starting at 2155, more systematic changes, affecting the storm as a whole, became evident. An increasing volume of radar echo at mid- and upper levels was occupied by weakly upward-moving air, and an increasing volume of radar echo at lower levels was occupied by downward-moving air (Fig. 4).

The vertical velocity distributions contained two populations of downdrafts: one at upper levels and one at lower levels. This characteristic is evident in both the CFADs and mean profiles and was most distinct during the highly convective stage of the storm.

At the early stage of the storm (2123 UTC), the frequency distribution outliers indicate two peaks of upward vertical velocity: one at low levels and the other at upper levels near 9 km (Fig. 3b). As the convection became more energetic (2139 UTC), the lower-level peak of upward motion in the 5% m^{-1} s km^{-1} contour became less distinct, while the upper-level peak increased in magnitude and altitude (compare Figs. 3b and 3d). The strongest updrafts (indicated by the 5% m^{-1} s km^{-1} contour in Fig. 3d) were nearly 10 m s^{-1} at 10-km altitude. The local maximum in the mean downdraft profile at the 10-km altitude and w = -2 m s^{-1} was at almost the same level as the maximum in the mean updraft profile at the 10.4-km altitude and w = 5 m s^{-1} (Fig. 6b). The strongest downdrafts (5% m^{-1} s km^{-1} contour in Fig. 3d) were -6 to -4 m s^{-1} and were below the 6-km altitude. An indication that the lower-level downdrafts were precipitation-driven (Srivastava 1985, 1987) is that they had consistently higher mean reflectivities than lower-level updrafts (Fig. 5). However, in detail the point-to-point correlation between reflectivity and vertical velocity at low levels is weak, and high reflectivities are also present in some low-level updrafts (Figs. 13a and 13c of YH Part I).

At 2144 UTC, the CFAD of vertical velocity shows that the peak updrafts (5% m^{-1} s km^{-1} contour) were still concentrated aloft, reaching their maxima at 8–13 km (Fig. 3f). The 10% m^{-1} s km^{-1} contour indicates
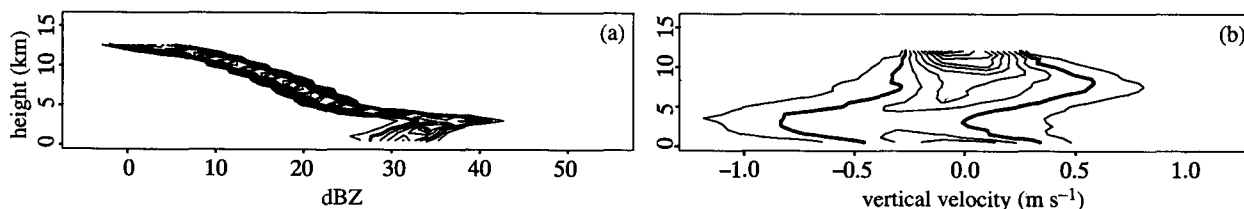
FIG. 8. CFADs of radar reflectivity (left) and vertical velocity frequency (right) from a stratiform volume observed to the rear of a Kansas squall line at 0345 UTC 11 June 1985 during the PRE-STORM project. (a) Radar reflectivity CFAD bin size is 2.5 dBZ, contoured at 5% dBZ^{-1} km^{-1} intervals, (b) vertical velocity CFAD bin size is 0.2 m s^{-1}, 50% m^{-1} s km^{-1} contour interval with 100% m^{-1} s km^{-1} contour highlighted. Note that (b) is plotted on a different horizontal scale than the CaPE CFADs of vertical velocity in Fig. 3.

several local maxima of updrafts in the frequency distribution, one below 5 km and two above 8 km. The 5% m^{-1} s km^{-1} contour also shows two concentrations of downdrafts with height (Fig. 3f). Downdrafts of approximately -5 m s^{-1} were most frequent at the 10–13- and at 2–5-km heights.

Although the strongest updrafts were weakening by 2155 UTC (compare 5% m^{-1} s km^{-1} contours in Fig. 3f and 3h), the volume of weaker and moderate strength updrafts at mid- and upper levels was increasing (compare Fig. 4b and 4c). More volume of the storm was moving upward at mid- and upper levels than previously but more slowly. Between 5 and 12 km in altitude, the contours in the domain 2 m s^{-1} < w < 4 m s^{-1} (Fig. 3h) are located at slightly higher vertical velocities (were shifted to the right) compared to their counterparts at 2144 UTC (Fig. 3f). The increased spacing between the contours indicates a broadening of the main peak in the frequency distribution topography of vertical velocity at mid- and upper levels toward these moderate updraft magnitudes. Below 5 km, the spacing between the contours in the vicinity of -1 < w < -2.5 m s^{-1} had become more uniform, representing a gentler slope in the frequency distribution topography of vertical velocity at lower levels and indicating an increased relative volume of weak downward motion at low levels also seen in Fig. 4c. The two populations of downdrafts had become less distinct in the mean profile (Fig. 6d) as the altitude of the local maximum corresponding to the upper-level downdrafts lowered. Additionally, the lower-level concentration of updrafts seen earlier in the distribution outliers had disappeared (Fig. 3f).

At the transitional stage of the storm (2237 UTC), the CFAD of vertical velocity shows a distribution of vertical velocities much narrower (-2 to 3 m s^{-1}) than at previous times (10% m^{-1} s km^{-1} contour in Fig. 3j). The trend toward increasing the relative volumes of upward-moving air above 5 km and downward-moving air below 5 km had continued (Fig. 4d). The majority of the storm volume exhibited weak downdrafts below 5 km and weak updrafts above 5 km as indicated by the steep peaks in the frequency distribution topography at lower and upper levels (Fig. 3j) and the percentage cumulative area less than 0 m s^{-1} at each height (Fig. 4d). The mean vertical velocity was about 0.5 m s^{-1} in the upper troposphere and about -0.1 m s^{-1} in the lower troposphere (Fig. 6e). At low levels, the absolute value of the mean vertical velocity within updrafts was slightly higher than within downdrafts (Fig. 6e). Thus, the negative value of the total mean vertical velocity at low levels was a result of the larger volume of downdrafts compared to the volume of updrafts at low levels (Fig. 4d). The shape of the mean vertical velocity profile for 2237 (Fig. 6e) has similarities to typical profiles in the stratiform regions of mesoscale convective systems (Fig. 1a). The weakening of the vertical velocity distribution into a strati-

form-like profile occurred gradually as the frequency distribution narrowed about 0 m s^{-1}. However, although the mean profile of vertical velocity is tending toward a stratiform character, the detailed velocity structure consists of many small-scale (a few kilometers wide) updrafts and downdrafts (Figs. 8e, 9e, and 10i,j of YH Part I). On the eastern and southern edges of the domain, the maximum updrafts were greater than 3 m s^{-1}, while in the trailing portion of the system most were closer to 1 m s^{-1} (Fig. 8e of YH Part I).

The CFAD of vertical velocity for the stratiform region of the PRE-STORM case (Fig. 8b) indicates a continuation of trends seen in the convective and transitional stages of the storm. The vertical velocity distribution was concentrated between -1 and 1 m s^{-1}, and was unimodal about the mean value. The frequency distribution of vertical velocity shows both updrafts and downdrafts at all levels. The general trend is for weak descent below the 0°C level and weak ascent above. Downdrafts of about -1.1 m s^{-1} and updrafts of about 0.8 m s^{-1} make up the outliers of the distribution. The CFAD more clearly shows what a mean profile cannot show—that the mesoscale drafts associated with stratiform areas are the net result of the ensemble of updrafts and downdrafts.

From the discussion above, it is becoming evident how the stratiform region in mesoscale convective systems develops (which is the goal of this study). The CFADs show that even in a stratiform region, the detailed vertical velocity structure consists of many small-scale updrafts and downdrafts. It is the combined behavior of these smaller-scale drafts that on average comprises the "mesoscale" updrafts and downdrafts seen in sounding composites (Gamache and Houze 1982, 1985; Houze and Rappaport 1984; Leary and Rappaport 1987), velocity–azimuth displays (Srivastava et al. 1986; Rutledge et al. 1988), and averages of dual-Doppler radar data (Smull and Houze 1987a; Biggerstaff and Houze 1993), none of which resolve the individual kilometer-scale drafts. It is only when the evolution of the statistical distribution of vertical velocity is viewed via the CFADs that the nature of the evolution from convective to stratiform structure is seen. The ensemble of updrafts and downdrafts, which began as relatively isolated structures, proceeds through a continuum of statistical states in which the smaller-scale drafts remain numerous but gradually weaken. Somewhat surprisingly, both updrafts and downdrafts are present at all altitudes at all times. The signal structure of vertical motion in the stratiform region—mesoscale downdrafts below the melting level and mesoscale updrafts above—is largely a matter of the downdrafts outweighing updrafts at low levels and updrafts outweighing downdrafts aloft; although in linear convective systems an additional larger-scale downdraft associated with rear-inflow (Zipser 1969, 1977; Houze 1977; Smull and Houze 1987b) can become organized and also contribute to the mean down-

ward motion at low levels (a factor that was true in the PRE-STORM case illustrated in Fig. 8b).

d. Relation of upper-level updrafts and upper-level downdrafts

Strong mid- and upper-level downdrafts have been reported previously (Heymsfield and Schotz 1985; Smull and Houze 1987a; Biggerstaff and Houze 1993; Knupp 1987; Kingsmill and Wakimoto 1991; Raymond et al. 1991; Smull and Augustine 1993; and others). However, no consensus has been reached on the mechanisms of upper-level downdraft origin. The high-resolution radar available from CaPE and its statistical presentation via CFADs provide a new perspective on this problem.

Anecdotal evidence from individual vertical and horizontal cross sections of the 15 August 1991 storm indicated the upper-level downdrafts were present throughout the radar echo volume and tended to be located next to mid- and upper-level updrafts (Figs. 7b, 8b, and 9b–d of YH Part I). Several upper-level downdrafts appeared to encircle a larger strong updraft in the horizontal cross section (Fig. 8b of YH Part I). The small contiguous areas of upper-level downdrafts (smaller than 16-km^2 area less than -2 m s^{-1} magnitude, Figs. 10a–e of YH Part I) are consistent with an interpretation of smaller downdrafts flanking a larger updraft. At mid- and upper levels, the weaker mean reflectivity within downdrafts, compared to within updrafts, is an indication that the upper-level downdrafts were not forced by precipitation drag (Fig. 13b of YH Part I and Fig. 5).

Statistical evidence of the ensemble kinematic properties of the entire storm, illustrated in the CFADs of vertical velocity (Figs. 3b,d,f,h), indicated that the upper-level downdrafts were vertically concentrated at levels that corresponded to the levels of the strongest upper-level updrafts. The level of the stronger upper-level downdrafts followed the level of the stronger upper-level updrafts upward from 8 to 10 km between 2123 and 2139 UTC (5% and 10% m^{-1} s km^{-1} contours in Figs. 3b,d). The level of the strongest upper-level downdrafts (5% m^{-1} s km^{-1} contour) lowered from roughly 11 km at 2144 to 9 km at 2155 UTC in concert with the stronger upper-level updrafts (10% m^{-1} s km^{-1} contour). This lowering of the level of stronger upper-level downdrafts following the level of the stronger upper-level updrafts is also evident in the mean profiles of the updraft and downdraft components of vertical velocity at 2144 (Fig. 6c) and 2155 UTC (Fig. 6d). The statistical relationship between the upper-level downdrafts and the updraft extrema in time and altitude is compelling evidence that the upper-level downdrafts and upper-level updrafts were dynamically related.

In combination, the points above present strong evidence for the hypothesis (Heymsfield and Schotz 1985; Smull and Houze 1987a) that the upper-level downdrafts are mechanically forced. By mechanically forced, we mean that, as explained by Houze (1993, chapter 7), the upper-level downdrafts are forced by the pressure gradient forces required to maintain mass continuity in the presence of buoyant parcels. (See appendix B for a mathematical summary of this concept.) The pressure gradient forces associated with rising parcels produce localized convergence in the adjacent environmental air by accelerating air laterally away from the tops of buoyant parcels. In other words, the upper-level downdrafts are a consequence of the buoyancy perturbation pressure field associated with the buoyant updrafts and mass continuity.

The competing hypotheses for the primary mechanism forcing upper-level downdrafts do not fully account for the observational evidence presented above. The theory of penetrative downdrafts was originally derived by Squires (1958) to explain flight-level aircraft observations of unsaturated downdrafts and was expanded upon by Paluch (1979) and Emanuel (1981). The penetrative downdraft theory states that upper-level downdrafts are created at cloud top by turbulent mixing with drier air and driven by evaporative cooling. They are not necessarily tied to strong updrafts. The changes in altitude of the upper-level downdrafts following the levels of the strongest upper-level updrafts are not fully explained by mixing with drier air at cloud top. The idea that the upper-level downdraft is forced by the buoyancy perturbation associated with the updraft itself fits the observations more closely since it requires that the upper-level downdrafts occur at the same times and heights as the strong updrafts. Although mixing of drier air at cloud top certainly does occur and may augment upper-level downdrafts, it probably is not the primary mechanism behind upper-level downdrafts.

Modeling studies by Rotunno and Klemp (1982) have shown that the interaction of strong vertical wind shear with an updraft creates a low pressure perturbation downshear of the updraft that draws drier environmental air into the storm and creates a negative thermal buoyancy that forces an upper-level downdraft. Observational evidence presented in this study shows that this mechanism cannot be extended to cases of weak vertical wind shear (Kingsmill and Wakimoto 1991) since this theory does not explain why upper-level downdrafts are pervasive throughout the storm and can occur on both the upshear and downshear sides of updrafts. Again, wake entrainment effects may occur to augment upper-level downdrafts, but in cases of weak vertical wind shear they do not appear to be the primary mechanism forcing them.

4. Differential reflectivity measurements

In this section we extend the discussion of the microphysics of the storm by examining the distribution

of differential reflectivity Z_{DR}. Differential reflectivity aids the physical interpretation of the microphysical evolution by providing information on the shapes and types of particles.

a. Characteristics of the data

Dual-polarization radars are designed to transmit and receive at vertical and horizontal polarizations. Radar reflectivity information from the two orthogonally polarized signals can be combined into a single variable called the differential reflectivity (Seliga and Bringi 1976), which is defined as

$$Z_{DR} = 10 \log \left(\frac{Z_{HH}}{Z_{VV}} \right), \tag{1}$$

where Z_{HH} is the horizontally transmitted, horizontally received radar reflectivity and Z_{VV} is the vertically transmitted, vertically received radar reflectivity. The differential reflectivity differs from reflectivity in that it is not as sensitive to particle concentration (because it is based on the ratio of reflectivities). Differential reflectivity provides information about the typical shape of the largest particles in the resolution volume being sampled since Z_{DR} is based on radar reflectivity, which is proportional to the sixth power of the diameter of the reflecting particles. If the particles are nonspherical and have a preferred spatial orientation, they exhibit a nonzero Z_{DR}. Differential reflectivity is an indicator of ice versus water phase (Hall et al. 1980, Hall et al. 1984; Seliga et al. 1981).

A brief review of guidelines for interpreting differential reflectivity observations is given in appendix C. To summarize, positive Z_{DR} is an indicator of rain; the larger the value, the larger the drops. High values of Z_{DR} in a thin layer near 0°C mark the melting layer. Near zero Z_{DR} is associated with ice aggregates or small particles. Negative values of Z_{DR} are associated with vertically oriented particles, probably graupel. Since these associations are not unambiguous, interpretation of Z_{DR} values needs to be made in the context of other observations.

Three volumes of polarimetric data from CP-2 that closely correspond to the times of the first three dual-Doppler volumes are used to indicate the differential reflectivity structure. The greater distance of the CP-2 radar from the study area (60–100 km) results in a coarser effective resolution for the differential reflectivity data compared to the corresponding data from the C-band radars, which were, at maximum, 55 km from the edge of the dual-Doppler box (Fig. 1b of YH Part I).

CP-2 polarimetric data were processed through NCAR RDSS (Oye and Carbone 1981) to take into account calibration and bias corrections in the Z_{DR} field. Interpolation of the Z_{DR} data to the same Cartesian grid as the dual-Doppler data was done using NCAR RE-

ORDER since some of the volumes were scanned by the antenna moving vertically and others were scanned by the antenna moving horizontally. Data were then input into NCAR CEDRIC (Mohr and Miller 1983), and a set of thresholding steps was employed to remove problematic data (Herzegh and Jameson 1992). Thresholding was designed to retain only the most reliable data (i.e., data within the main body of the storm that did not have anomalous values). Data were retained at the grid point if the corresponding C-band reflectivity value was greater than 10 dBZ, the Z_{DR} values were between -1 and 5 dB, and a dual-Doppler vertical velocity datum existed. As a measure of quality control, the reflectivity field from CP-2 was compared to the reflectivity field from the C-band radars. The fields matched closely with the small differences present attributable to the slight difference in times and resolutions of the volumes.

b. Spatial variability of Z_{DR}

To illustrate some features of the Z_{DR} spatial structure, cross sections of the Z_{DR} field at 2139 UTC are shown in conjunction with the corresponding vertical velocity and reflectivity fields from the C-band dual-Doppler analysis in Fig. 9. The horizontal cross section at 2.8 km (Fig. 9a) shows a continuous area of positive Z_{DR} occupying most of the area of the storm, indicating rain falling within the area of the radar echo. The highest Z_{DR} values are located behind the eastward-moving leading edge of the storm. This spacing indicates a time lag between new cell initiation and precipitation fallout at low levels. In contrast, the horizontal cross section at 8 km (Fig. 9b) shows Z_{DR} values near zero or negative. These Z_{DR} values are indicative of ice. The more negative values (<-0.5 dB), which indicate vertically oriented ice, tended to occur in the regions of strong updrafts and downdrafts (see overlaid contours of w in Fig. 9b). The vertically oriented ice in these areas was likely graupel. The Z_{DR} values close to zero (± 0.5 dB) were present in the more quiescent areas of the storm.

The vertical cross sections in Figs. 9c and 9d are taken along the 25-km-long line indicated in Fig. 9a and are centered on the same updraft (at $x = -14.5$ km, $y = -17$ km) as the cross sections in Figs. 7b and 7c of YH Part I. Reflectivity values > 40 dBZ in the region of the more negative (<-0.5 dB) Z_{DR} values between points C and D along the vertical cross section in Fig. 9d are a further indication of graupel. Additional evidence of graupel within the storm comes from aircraft measurements. The SDSMT T-28 aircraft observed graupel during its flight within this storm at the 5-km altitude (Detweiler and Smith 1992). The vertical cross section shows a varying maximum height of positive Z_{DR} values (>0.5 dB). Positive Z_{DR} values extended from the surface to the 5-km altitude on the west (trailing) side of the storm, to the 7-km altitude in the region of the strongest updrafts and downdrafts in this
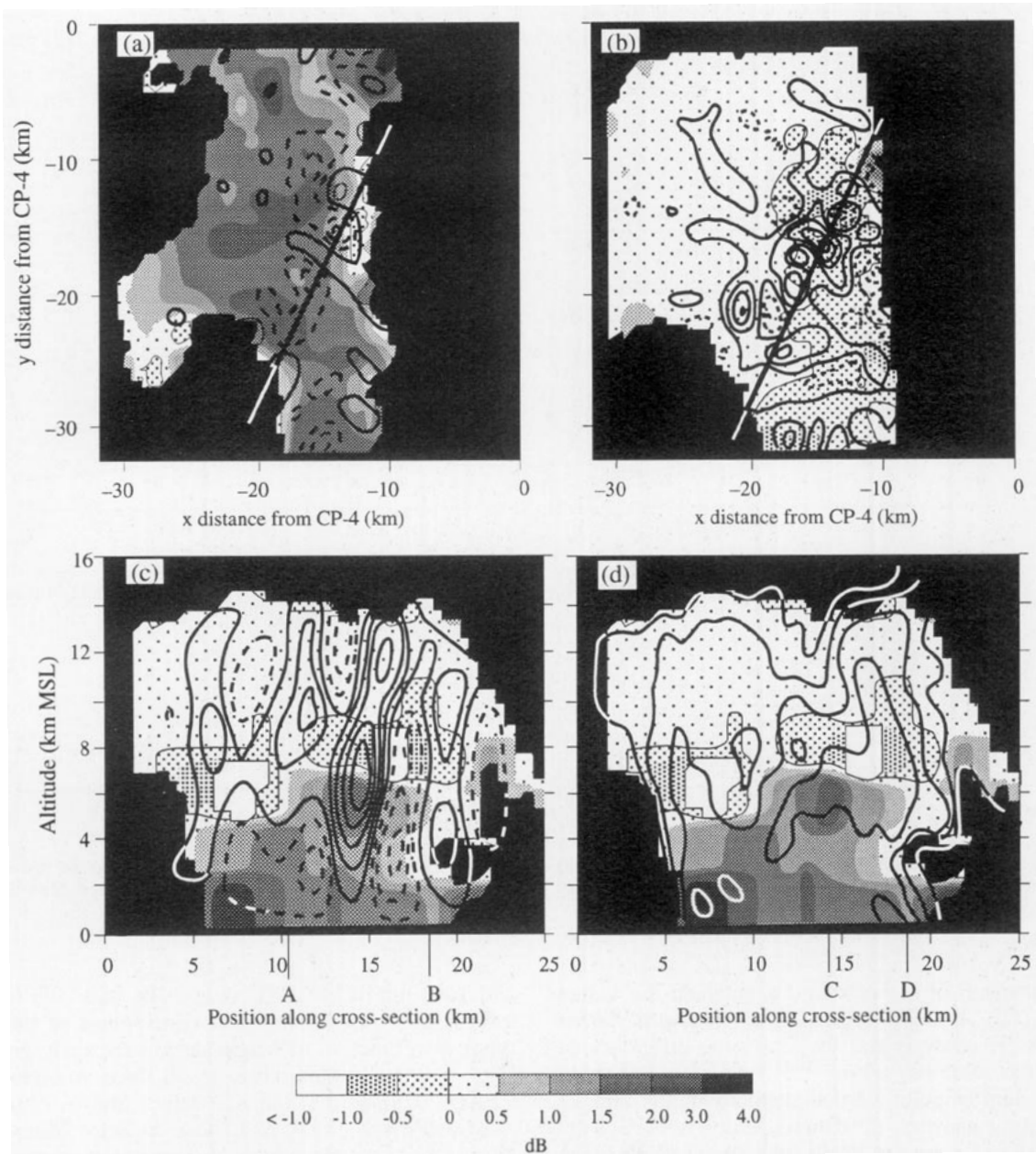
FIG. 9. Cross sections of Z_{DR} (from CP-2) through 2139 UTC volume. Heavy line in horizontal cross sections indicates location of vertical cross sections (25 km long). The Z_{DR} shading is indicated by the bar at the bottom of the diagram. Horizontal locations A, B, C, and D indicated along the bottom of the vertical cross section are referred to in text. (a) Horizontal cross section at the 2.4-km altitude, (b) horizontal cross section at the 8-km altitude, (c) vertical cross section along the straight line indicated in (a) and (b), vertical velocity (from dual-Doppler analysis) contours at -9, -3, 3, 9, 15, 21, 27, and 33 m s^{-1} are superimposed, negative values are dashed. (d) Same as (c) except reflectivity (from C-band radars) contoured at 10-dB intervals starting at 20 dBZ are superimposed.

cross section ($x = A$ to $x = B$ in Fig. 9c), and to 2 km at the eastern (leading) edge of the storm. Columns of Z_{DR} values greater than 1 dB extending a few kilometers above the environmental 0°C level in convective storms have been interpreted as supercooled raindrops lifted by updrafts (Hall et al. 1984; Illingworth et al. 1987; Tuttle et al. 1989). Bringi et al. (1993) noted a correspondence between selected regions of elevated Z_{DR} and the locations of updrafts inferred from aircraft flight-level winds. The cross section superimposing the dual-Doppler velocity analysis on the Z_{DR} field (Fig. 9c) indicates, however, that the elevated positive Z_{DR} values are not located strictly within the updrafts. Some uncertainty about this conclusion remains as a result of
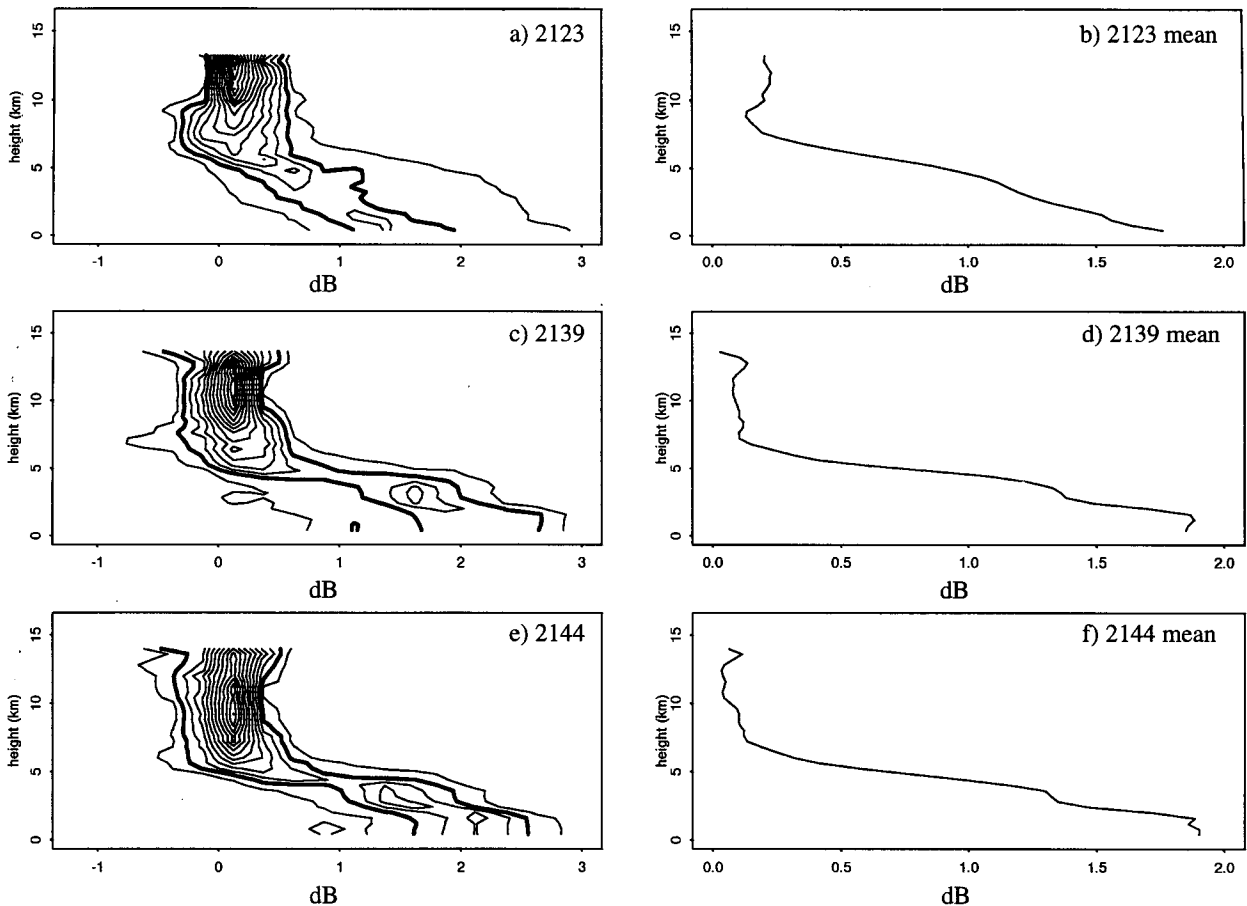
FIG. 10. Times series of CFADs of Z_{DR} frequency (left column) and mean vertical profiles of Z_{DR} (right column). CFAD bin size is 0.25 dB. CFADs are contoured at 50% of data per decibel per kilometer intervals with the 100% dB^{-1} km^{-1} contour highlighted. Note that the abscissa scales are different.

the mismatch of the resolutions between the C-band radars (CP-3 and CP-4) and the CP-2 radar in the volume under analysis and the start time difference between the volumes (~ 1 min). Further comparisons between dual-Doppler vertical velocity fields and Z_{DR} measurements where the data resolution is more closely matched are needed to resolve the association between the areas of elevated positive Z_{DR} and updrafts and downdrafts over an entire storm volume. The coarse spatial resolution of the Z_{DR} data in this analysis over-estimates the volume of the storm occupied by Z_{DR} > 1 dB.

c. CFADs of differential reflectivity

The CFADs and mean profiles of differential reflectivity at 2123[10] (Figs. 10a and 10b), 2139 (Figs. 10c

---

[10] The CP-2 volume scan from 2122:56 to 2125:56 UTC did not extend above the top of the storm. Consequently, Figs. 10a and 10b are truncated at the top.

and 10d), and 2144 UTC (Figs. 10e and 10f) reveal information on the statistical distribution of particle types as a function of height during the early growth stage of the cumulonimbus. In all three volumes, the CFADs indicate that the Z_{DR} values above 5 km are most frequently weak and close to zero. More precisely, the peak frequency of occurrence is near 0.2 dB^{11} for levels above 5 km. This result is remarkably consistent within and among the CFADs in Fig. 10. The peak in the distribution at low Z_{DR} values is indicative of aggregates of low bulk density and/or small precipitation-sized[12] ice particles of no preferred spatial orientation. The probability of occurrence of aggregates generally decreases with decreasing temperature

---

[11] This does not appear to be an artifact of the data processing. Correction for instrument bias errors has been incorporated into the data.

[12] Radar measures echo from precipitation-sized particles (>0.1 mm). Cloud droplets are generally below the detectable threshold for the radars used in this study.

(Hobbs et al. 1974). Thus, the distribution of particles with near-zero Z_{DR} is more likely to include larger aggregates at midlevels and other types of precipitation-sized ice particles at upper levels. The associated reflectivity distributions above 5 km are predominantly below 35 dBZ (Figs. 3a,c,e). The reflectivity distribution thus corroborates the interpretation that the majority of precipitation-sized ice particles consisted of snow[13] rather than graupel or hail (Straka and Zrnić 1993). Above 5 km, the outliers in the CFADs of reflectivity greater than 35 dBZ (Figs. 3a,c,e) and the outliers in the CFADs of differential reflectivity (Figs. 10a,c,e) with stronger negative Z_{DR} values indicate that a small number of the precipitation-sized particles at these altitudes were graupel.

These conclusions are a further indication of the usefulness of the CFAD for the analysis of radar data. From Figs. 9a and 9b it is possible to determine from the primary mode of the distribution that aggregates are the dominant type of particle between 5 and 10 km. The outliers of the distribution indicate that the storm volume between 5 and 10 km also contained some graupel at certain altitudes (where $Z_{DR} < 0$) and some supercooled raindrops (where $Z_{DR} > 0.5$). The full frequency distribution in the CFAD provides much more information than the mean Z_{DR}, which only indicates the dominant particle type.

At 5 km, near the environmental 0°C level, there is an abrupt shift of the peak frequency in the CFADs of differential reflectivity from values of near 0 dB at higher levels, which are indicative of snow, to values greater than 1 dB at lower levels. Differential reflectivity values exceeding 1 dB indicate that the larger particles present were predominantly horizontally oblate raindrops. This observed shift in the frequency distribution of Z_{DR} values between ice and liquid water regimes has some similarities to that observed by Seliga and Aydin (1983) in unglaciated and glaciated clouds in Montana. Below 5 km, the peak frequency in the Z_{DR} distribution slopes diagonally, such that Z_{DR} increases in value with decreasing height. The downward increase in Z_{DR} indicates increasing average drop size for the largest drops (Figs. 10a,c,e). At 2139 and 2144 UTC, there is a break in the diagonal slope of the frequency distribution contours (Figs. 10c,e) toward a more vertical slope near 2 km. Fulton and Heymsfield (1991) saw a similar phenomenon in their Alabama storm core data. The break in the slope of the frequency distribution may be an indicator of a limit on drop growth. Additionally, below 5 km, the frequency of the lower Z_{DR} values (between 0 and 1 dB) decreases with decreasing height since the radar return was domi-

nated by the larger raindrops associated with larger Z_{DR} values.

The mean Z_{DR} values (Figs. 10b,d,f) show a gradual transition of increasing Z_{DR} with decreasing height in the region around the melting level (between 7 and 3 km). The mode of the Z_{DR} distributions as represented by the peak in the CFADs of Z_{DR} (Figs. 10a,c,e) retains the melting-level discontinuity better than the mean since it exhibits a sharper discontinuity at the height of the melting level than does the mean differential reflectivity profiles (Figs. 10b,d,f).

The ensemble properties of differential reflectivity indicate that snow (including both aggregates and other precipitation-sized ice particles) predominated above 5 km even at the early stages of the storm (2123 UTC, Fig. 10a). This evidence of early glaciation indicates cold-cloud processes were important in the production of precipitation from the initial stages of the storm. This fact does not imply that warm rain processes (i.e., collision-coalescence) were not also contributing to the precipitation. However, they must have occurred in concert with riming and aggregation throughout the time the storm was observed by radar.

5. Microphysical evolution of the storm

This section synthesizes the information on reflectivity and differential reflectivity (Figs. 3, 5, and 10) to describe how the profile of mean reflectivity in convective conditions evolves into the profile of mean reflectivity in stratiform regions (Fig. 1b).

a. Reflectivity structure near the 0°C level

The evolution of the mean reflectivity profile in the storm under study may be characterized to a large extent by the behavior of the reflectivity in the vicinity of the 0°C level. This behavior is expected to differ depending on whether the precipitation particles observed by radar are ascending or descending. Ascending precipitation-size raindrops carried by updraft parcels above the environmental 0°C level do not all freeze instantaneously[14] (Rogers and Yau 1989). Supercooled raindrops may be found above the 0°C level (Hallett et al. 1978). In convective storms, supercooled raindrops are associated with strong updrafts (e.g., Illingworth et al. 1987; Tuttle et al. 1989; Fulton and Heymsfield 1991; Bringi et al. 1993). In section 4, we showed by means of the differential reflectivity data that supercooled raindrops were likely present in the 15 August 1991 storm.

Once ice appears, glaciation occurs rapidly (Hallett et al. 1978). Contact nucleation and the lower vapor

---

[13] Snow is defined here, following Houze (1993), as precipitation-sized ice particles with terminal fall speeds between about 0.3 and 1.5 m s^{-1}. These particles may be pristine crystals, larger fragments of particles, rimed particles, or aggregates.

[14] Homogenous nucleation occurs near −40°C. Hence, heterogeneous nucleation (likely contact nucleation) is the primary mechanism responsible for freezing raindrops at warmer temperatures (Hobbs 1974).

pressure of ice compared to water act rapidly to freeze and/or evaporate the remaining precipitation-sized liquid water drops. Thus, within updrafts there is a "glaciation zone" between the environmental 0°C level and the level where the precipitation-sized hydrometeors are primarily ice. The depth of the glaciation zone can extend a few kilometers above the environmental 0°C level and is dependent on the speed of the updrafts, the presence of preexisting ice, and the convective available potential energy (CAPE)[15] of the storm. The speed of updrafts and the presence of preexisting ice are related to the stage of storm evolution, and the CAPE is a function of the prestorm environment.

The associated reflectivity profile of descending particles reflects changes in their size, phase, and concentration during descent. Descending ice particles present in downdrafts or very weak updrafts may grow by aggregation, riming, or deposition, and their associated reflectivity may correspondingly increase as they descend. As precipitation-sized ice particles cross the 0°C level, they melt[16] within a thin layer of atmosphere. This melting produces a very high radar reflectivity maximum just below the 0°C level. A rapid transition from the lower reflectivity values characteristic of ice to the higher reflectivity values associated with melting ice is reflected in the reflectivity profile for descending ice particles. In stratiform precipitation, the mean reflectivity drops off again below the melting layer, and the melting layer appears as a bright band on radar (Houze 1993, 200–202). In convective precipitation, the mean reflectivity below the melting layer may be higher, lower, or the same as that in the melting layer.

b. Interpretation of observed mean reflectivity profiles with the aid of CFADs of reflectivity, differential reflectivity, and vertical velocity

Physical interpretation of the evolving profiles of mean reflectivity in the 15 August 1991 storm is aided by decomposition of the total mean profile into updraft and downdraft components (Fig. 5). In regions of ice particles (above 5 km), the mean reflectivity within updrafts was higher than within downdrafts. The lower reflectivity in downdrafts is probably related to the unfavorable conditions for ice particle growth in downdrafts (Braun and Houze 1994). Sublimation and evap-

---

[15] The CAPE (Houze 1993, p. 283) of a storm is a function of the temperature difference between environmental air and the air in a parcel lifted from the surface. The larger the temperature difference between ambient air and the air within rising parcels in the vicinity of the 0°C environmental level, the potentially deeper the glaciation zone.

[16] Hail and graupel, reaching the ground, obviously do not melt completely, but by definition all other ice does. Although graupel was noted by aircraft (e.g., SDSMT T-28) within this storm, no hail or graupel was reported on the ground (J. Wilson 1992, personal communication).

oration within downdrafts may also act to lower reflectivity.

The uppermost altitude at which a local maximum in reflectivity occurred in the downdraft mean reflectivity profile remained fairly stationary near the 4-km altitude throughout the evolution of the storm (Fig. 5). This maximum was evidently related to the melting of descending particles. It occurs at the height where the CFAD of Z_{DR} exhibits a sharp discontinuity clearly associated with melting (Fig. 10).

In contrast, the local maximum of reflectivity in the updraft mean reflectivity profile was at 6 km in altitude at 2123 UTC and progressively sank to near 4 km by 2237 UTC. Additionally, the depth of the glaciation zone (from the environmental 0°C level of 4.4 km to the level where reflectivity begins to decrease sharply with increasing height) was largest at 2123 (Fig. 5a) and narrowed with time. At 2155, the local maximum in reflectivity dropped close to 4.4 km, indicating that the glaciation zone had essentially disappeared (Fig. 5d). The difference in altitudes between the local maxima in the mean profiles of updraft and downdraft components was greatest in the early stages of the storm.

The narrowing of the apparent glaciation zone as the storm evolved and the accompanying decrease in prevalence of supercooled raindrops in strong updrafts can be seen in the CFADs of both reflectivity (Fig. 3) and Z_{DR} (Fig. 10). In Fig. 3, the height of the maximum reflectivity in the 2.5% dBZ^{-1} km^{-1} contour lowers as the storm evolves. The two peaks in the overall topography of the Z_{DR} frequency distribution (Fig. 10), in ice centered at the 10-km altitude and 0.2 dB and in rain centered at 3-km altitude and 1.6 dB, became more distinct as the storm evolved and the diagonal ridge in the frequency distribution topography connecting the two regions narrowed (Figs. 10a,c,e). The area of the frequency distribution topography in Fig. 10 that was reduced with time (Z_{DR} values greater than 0.5 dB above the environment freezing level) corresponds to points in the frequency distribution that are likely associated with supercooled raindrops. The collapse of the glaciation zone indicates that as the storm evolved, proportionately smaller areas within the storm were occupied by supercooled raindrops. However, relative to the volume of the storm as a whole, the volume occupied by supercooled raindrops was always small, consistent with the low frequency of updrafts greater than 10 m s^{-1} in the vertical velocity distributions in Figs. 3 and 4. The relative volume of supercooled drops decreased from 2123 to 2144 UTC (Figs. 10a,c,e), while the magnitude of the strongest vertical velocities (Figs. 3b,d, f), which could loft the supercooled drops higher and thus potentially increase the depth of the glaciation zone, increased during that time. Thus, the preexistence of ice was evidently the key factor in the collapse of the glaciation zone, not the changing vertical velocity distribution.

In the early stages of the storm, when the glaciation zone was deeper, the updrafts were penetrating quiescent air that contained no preexisting particles. As the storm matured, more ice was present aloft and most was drifting downward between the strong updrafts. The increased concentration of ice particles in the air penetrated by new updrafts apparently aided in the more rapid freezing of the supercooled raindrops by providing more opportunities for contact ice nucleation.

As the storm matured further and the distribution of updrafts weakened, more of the particles in a given updraft parcel were falling through rather than being suspended, and the reflectivity profile for updrafts progressively resembled a reflectivity profile characteristic of falling particles (similar to the profile within downdrafts), which resembles the typical stratiform profile. The beginning of the stratiform stage might be defined as the time when almost all the precipitation-size particles within the updraft parcels are falling. The difference between mean reflectivity profiles in updrafts and downdrafts was reduced as the storm aged (Fig. 5). In the case of the storm under study, by 2237 UTC (Fig. 5e) updraft and downdraft profiles of mean reflectivity were almost identical. The transition in the shape of the mean reflectivity profile at midlevels from convective (gentle local maximum) to stratiform (sharp local maximum) was thus a result of the reflectivity in the storm at midlevels being dominated by ascending particles (wide glaciation zone) in the initial stages of the storm and by falling particles (narrow melting layer) in the later stages of the storm.

The overall weakening of the mean reflectivity profile during the convective-to-stratiform transition (Figs. 1b, 5d, and 5e) was related to the weakening vertical velocity during the transition. The larger more reflective precipitation-size particles were present and fell out during the earlier convective stages of the storm (section 3b). The smaller, more slowly falling precipitation-size particles were left to fall out during the intermediary and stratiform stages of the storm.

At lower levels, the mean reflectivity in downdrafts was always higher than in updrafts (Figs. 5a–e) and dominated the overall mean for the lifetime of the storm. These higher reflectivities were evidently associated with the more numerous and larger falling precipitation-size particles within downdrafts. The maximum reflectivity of raindrops appears to have been related to the reflectivity of precipitation-size ice particles that were melting into raindrops. In the convective period of the storm, when the distribution of updraft vertical velocity was wider, the distribution of reflectivity values in ice extended to over 40 dBZ and rain reflectivities were over 50 dBZ (Figs. 3a,c,e,g). At the intermediary stage of the storm, when the distribution of updraft vertical velocities was narrow, maximum reflectivity values in ice were less than 35 dBZ and maximum values in rain were less than 42 dBZ (Fig. 3i).

6. Conclusions

Examination of high-resolution radar data collected in Florida during CaPE has shed light on the nature of the evolving kinematic and microphysical processes occurring during the transition of a multicellular storm from a convective to stratiform state. Previous studies, using lower-resolution data, have characterized the mean properties of the convective and stratiform stages of the storm (e.g., Fig. 1). In this study, high-resolution radar data have permitted an examination of the small-scale variability within the storm, which as an ensemble combines to form the mean properties.

The changing ensemble properties of radar reflectivity and vertical velocity throughout the evolution of the storm were examined using CFADs (statistical distributions as functions of height) at a series of times (Figs. 3 and 8). The distribution of reflectivity above the 0°C level in the early stages of the storm indicated a heterogeneous mixture of ice particle types, sizes, and concentrations. The frequency distribution topography rapidly began to narrow into a diagonal of nearly homogenous reflectivity at each level and increasing reflectivity with decreasing height (Fig. 3). Nearly homogenous reflectivity at each level and increasing reflectivity with decreasing height above the 0°C level are characteristic of stratiform regions, yet by viewing the data statistically in CFADs we have determined that this stratiform microphysical structure actually began to appear during the kinematically most active stage of the storm. The origin of this reflectivity distribution was related to the distribution of vertical velocity. At all times, the most common values of vertical velocity distributed within the radar echo volume were weak. The strongest vertical velocities ($w > 10$ m s^{-1}) occupied only a small fraction of the volume of the storm. Thus, most of the hydrometeors injected aloft (by the stronger updrafts) were falling and growing in an environment of weak vertical velocity. Hence, the radar echo aloft began to take on a statistically stratiform structure early in the storm's lifetime. The statistically stratiform structure brought out by the CFADs is not readily apparent in instantaneous spatial cross sections.

Two types of downdrafts were present. Lower-level downdrafts were evidently precipitation-driven. Statistical evidence from the CFADs of vertical velocity (Fig. 3) indicates that the upper-level downdrafts were dynamically related to upper-level updrafts. The notion that upper-level downdrafts are a consequence of pressure gradient forces required to maintain mass continuity in the presence of buoyant updrafts more closely fits the observations than other hypotheses.

As the storm matured, progressively more of the volume of the storm at low levels was occupied by downward-moving air, and progressively more volume at upper levels was occupied by upward-moving air (Fig. 4). A stratiform-like dynamical structure became evident in the intermediary stage, even though this stage

was still characterized by many updrafts with $1 < w < 4$ m s^{-1}. The distribution of vertical velocity indicates that at all phases of storm evolution, including the stratiform stage, there are both updrafts and downdrafts at all levels. The mesoscale drafts associated with a stratiform region are the net result of the ensemble of updrafts and downdrafts.

The ensemble properties of the observed differential reflectivity were examined as a means to gain additional information on the microphysical characteristics of the storm (Fig. 10). The storm was glaciated early in its life cycle. In all three of the convective stage volumes analyzed, the differential reflectivity data showed that above 5-km altitude snow (aggregates and other precipitation-size ice particles) predominated. Small amounts of graupel were likely present above 5-km altitude in association with the more kinematically active areas of the storm. There was also evidence that small volumes of the storm above the 0°C level contained supercooled raindrops and that the relative volume occupied by the supercooled raindrops decreased rapidly as the storm matured from early to vigorous convective stages. The abrupt shift in the peak frequency of differential reflectivity in the CFADs of differential reflectivity (Fig. 10) graphically illustrates the rapid change with height between the snow and rain in the storm.

Examination of the CFADs of reflectivity, vertical velocity, and differential reflectivity and the subdivision of the mean profiles of reflectivity into updraft and downdraft components has allowed us to understand some of the subtle changes that the mean reflectivity profiles underwent as the storm evolved from a convective toward a stratiform structure. The shape of the mean profile of reflectivity underwent particularly significant changes at midlevels during this transition. In the convective stages of the storm, the shape of the mean reflectivity profile at midlevels was dominated by ascending particles freezing in a 1–2-km-deep glaciation zone. In later stages of the storm, the melting of falling particles in a shallow layer dominates the mean reflectivity profile at midlevels. The overall weakening of the mean reflectivity profile is related to the evolution of the ensemble of updrafts. As the stronger updrafts weaken, the heavier particles fall out in tens of minutes, leaving the lighter, slowly falling particles with weaker reflectivity remaining.

The individual results brought out by the CFADs of reflectivity, vertical velocity, and differential reflectivity all point to the general insight that the kinematic conditions over a majority of radar echo volume are remarkably similar across different stages of storm evolution. At all stages of the storm evolution, most of the ice particles in the upper levels of the storm are drifting downward since they cannot be supported aloft by the predominant weak updrafts and downdrafts. The primary ice-phase precipitation growth processes active in these regions are vapor deposition, riming, and ag-

gregation of ice particles as they *fall*. What differentiates the convective from the stratiform stages of the storm is the presence of a few stronger updrafts occupying a small fraction of volume of the storm that generate precipitation-size ice particles and disperse them into the mid- and upper levels of the storm. As the storm matures, these stronger updrafts weaken, and if they are not replaced by new growth, the entire draft ensemble weakens to the point that no new large particles are produced within updrafts. As the storm transitions toward the stratiform stage, the microphysical evolution becomes dominated by the fate of the ice particles generated previously within the few strong updrafts.

The CFADs, which have proven valuable in this study, should now be applied to other storms. CFADs provide an objective way to compare the structures of different storms. By revisiting older datasets, such as the dual-Doppler radar data collected in PRE-STORM and MIST [microburst and severe thunderstorm field experiment, which was part of the Cooperative Huntsville Meteorological Experiment (Dodge et al. 1986)], new insights into the properties and evolution of previously studied mesoscale convective systems may be gained. The CFAD technique will also be useful for comparing radar data collected by several disparate platforms—such as ground-based, aircraft, ship, and satellite—looking simultaneously at the same storm but where the spatial location of the data will be difficult to overlay precisely.

In addition, the CFAD will be useful to verify results of three-dimensional cloud models with observations. It is difficult to reproduce the exact spatial configuration of updrafts and downdrafts of observations within a numerical model, and comparisons between cross sections of model output and observations tend to be subjective. Verifying that the numerical model is producing a similar frequency distribution of a variable with height to that of observations would strengthen the comparison.

The statistical trends in the CFADs during storm evolution may also be useful in aiding the classification of the stage of storm development of a volume of radar data. This classification methodology would have application both in research and in operations—as an aid in very short term forecasting. Additionally, as well as using the CFADs to characterize the ensemble properties of single storm volumes, CFADs can be applied to climatological radar data (such as those that should be provided by the TRMM [Tropical Rainfall Measuring Mission (Simpson et al. 1988)] satellite-borne radar and TRMM Ground Truth Program) to gain insights into precipitation processes.

The third part of this study, Yuter and Houze (1995b), will extend the discussion of the kinematic evolution of the storm by examining vertical mass transport and mass divergence. A self-consistent conceptual model that synthesizes the microphysical and

kinematic observations detailed in the entire three-part study and describes the convective-to-stratiform transition of the storm will also be presented.

APPENDIX A

Contoured Frequency by Altitude Diagrams (CFADs)

For a simple two-dimensional histogram of variable A such as Fig. 2a, the total number of points N_t is

$$N_t = \int_{-\infty}^{\infty} \frac{\partial N(A)}{\partial A} \, dA = N_{t_1} + N_{t_2} + \cdots, \quad (A1)$$

where N is the frequency distribution function, defined such that $[\partial N(A)/\partial A]dA$ is the number of observations of A in the range A to $A + dA$. The terms on the right-hand side of (A1) represent the number of points in a finite interval ΔA. They represent the area under one bar of the histogram:

$$N_{t_i} = \int_{A_i}^{A_i + \Delta A} \frac{\partial N(A)}{\partial A} \, dA, \quad i = 1, 2, \cdots. \quad (A2)$$

All histograms in this paper use a constant bin width ΔA, and the ordinate is labeled in values of frequency $N_{t_i}(\Delta A)^{-1}$.

In the three-dimensional plot in Fig. 2b, the total number of points N_T in the volume is

$$N_T = \int_{-\infty}^{\infty} \int_0^{h_{top}} \frac{\partial^2 N(A, z)}{\partial z \partial A} \, dz \, dA, \quad (A3)$$

where h_{top} is the height of storm top, and $N(A, z)$ is the frequency distribution function defined such that $[\partial^2 N(A, z)/\partial z \partial A]dz \, dA$ is the number of observations
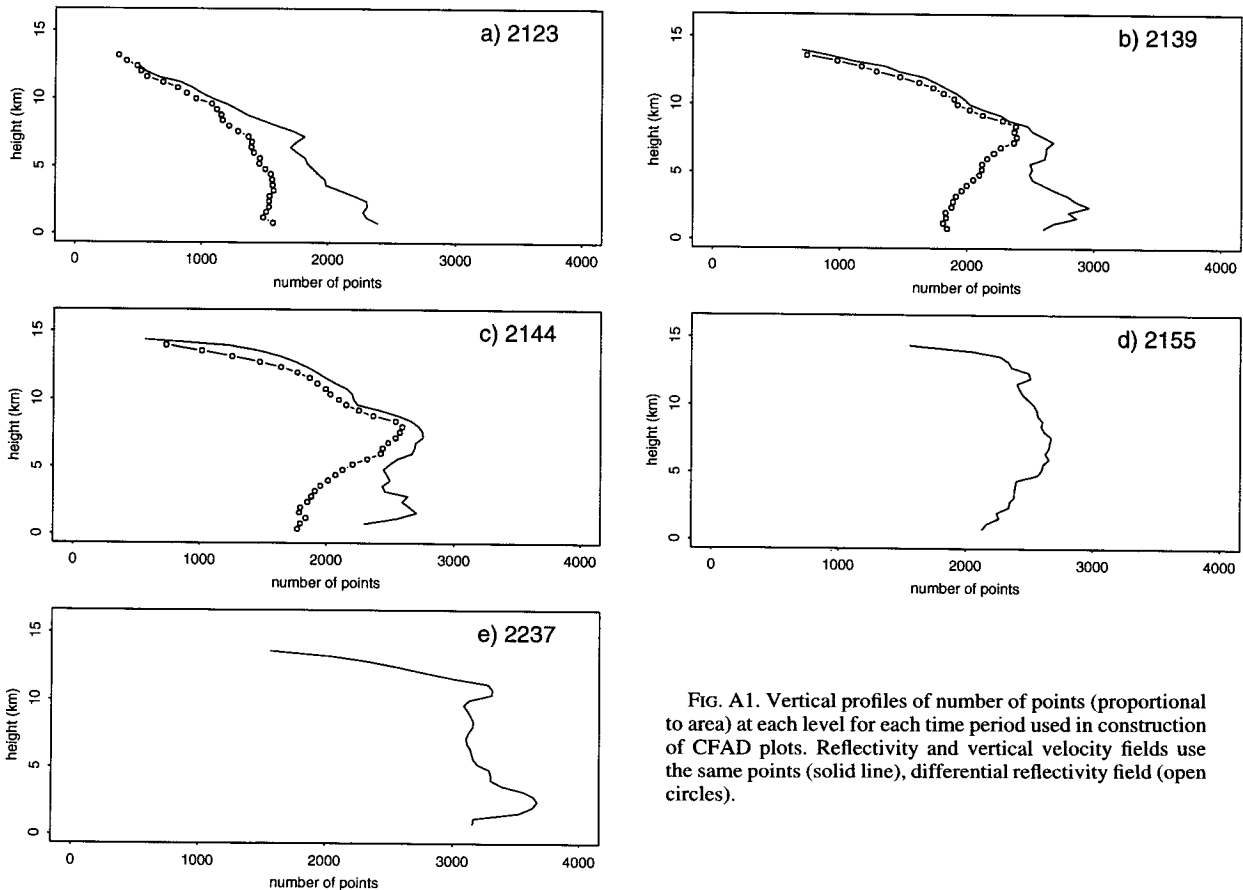

FIG. A1. Vertical profiles of number of points (proportional to area) at each level for each time period used in construction of CFAD plots. Reflectivity and vertical velocity fields use the same points (solid line), differential reflectivity field (open circles).

of A in the range A to $A + dA$ at heights in the range z to $z + dz$. Thus, the number of points in a bin defined by both A_i and z_j is

$$N_{T_{ij}} = \int_{A_i}^{A_i+\Delta A} \int_{z_j}^{z_j+\Delta z} \frac{\partial^2 N(A, z)}{\partial z \partial A} \, dz dA,$$

$$i = 1, 2, \cdots, \quad j = 1, 2, \cdots. \quad \text{(A4)}$$

A constant vertical bin size of $\Delta z = 0.4$ km is used corresponding to the interpolated Cartesian volume vertical grid spacing. Since both Δz and ΔA are constants, the frequency of occurrence of points per bin is $N_{T_{ij}}(\Delta z \Delta A)^{-1}$.

A further step in the creation of the CFAD is the normalization of the plot by the number of points at each level. The total number of points in each bin [Eq. (A4)] is divided by N_{z_j}, the number of points at level z_j, and then multiplied by 100 to express the fraction as a percent. Normalizing by the number of points at each level has the side effect of increasing the percentages at the top of the storm where there are fewer points, but it makes it easier to compare these diagrams between volume times and to plots of mean value versus height. Levels where the number of available data points are too few to be representative of the storm structure (less than 10%–20% of the maximum number of points at one level in the volume), such as those at the very top of the radar echo, are removed from the plot.

In the course of developing these plots, a variety of different histogram bin sizes, bin centers, and contour intervals were tried. Bin size was determined as a compromise among the error in calculations, significance of the amount of data in a bin, and the amount of detail revealed. In all the CaPE CFADs, $\Delta z = 0.4$ km, corresponding to the grid resolution in the vertical. For the reflectivity plots, a bin size of 5 dB captures the main patterns. Reducing the bin size changes some details but not the overall picture. A bin size of 0.25 dB is used for the Z_{DR} CFADs. For vertical velocity, a bin size of 2 m s^{-1} would define the main pattern in the more vigorous convective stage, but as the storm weakens, a bin size of 1 m s^{-1} is needed to clarify the pattern. A bin size of 1 m s^{-1} is therefore used for all the CFADs of vertical velocity in Fig. 3.

Figure A1 shows the number of points for each variable at each level in each time period used. The thresholding procedure for the Z_{DR} data, described in section 4, reduces the number of Z_{DR} data points at each level relative to the number of points in the reflectivity field.

APPENDIX B

Upper-Level Downdraft Dynamics

Buoyancy of a parcel of finite width and depth cannot exist without a simultaneous disruption of the pressure field. The resulting pressure field can be described mathematically by combining the three-dimensional equation of motion and the conservation of mass.

If friction and Coriolis force are ignored (a useful approximation for conditions inside a cumulonimbus), the Eulerian form of the equation of motion is

$$\frac{\partial \mathbf{V}}{\partial t} = -\frac{1}{\rho_0} \nabla p^* + B\mathbf{k} - \mathbf{V} \cdot \nabla \mathbf{V}, \quad \text{(B1)}$$

where $\mathbf{V}$ is the three-dimensional wind, ρ_0 is the base-state density (a function of height z only), p^* is the perturbation pressure, and B is the buoyancy.

Mass conservation under anelastic conditions is expressed by the continuity equation

$$\nabla \cdot \rho_0 \mathbf{V} = 0. \quad \text{(B2)}$$

The two equations can be combined by multiplying Eq. (B1) by ρ_0 and then taking the divergence of the result. Since $\nabla \cdot \rho_0 \mathbf{V} = 0$, the time derivative in the resulting equation is removed, leaving the diagnostic equation

$$\nabla^2 p^* = \frac{\partial(\rho_0 B)}{\partial z} - \nabla \cdot (\rho_0 \mathbf{V} \cdot \nabla \mathbf{V}). \quad \text{(B3)}$$

Equation (B3) shows that the divergence of the pressure gradient perturbation field ($\nabla^2 p^*$) in an anelastic fluid must be consistent with the vertical gradient of buoyancy [a buoyancy forcing (F_B)] and the three-dimensional divergence of the advection field [a dynamic forcing (F_D)]

$$\nabla^2 p^* = F_B + F_D. \quad \text{(B4)}$$
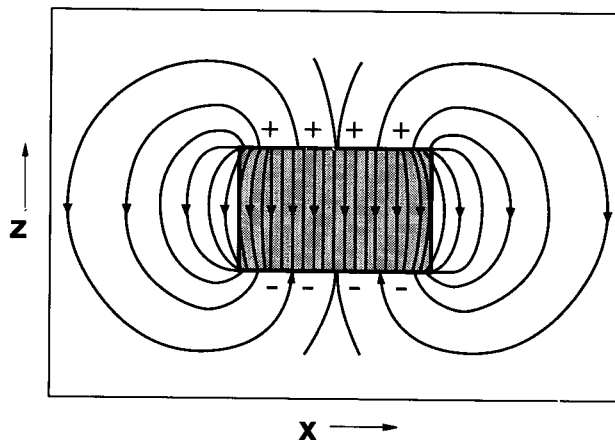
FIG. B1. Vector field of buoyancy pressure gradient force for a uniformly buoyant parcel of finite dimensions in the x–z plane obtained by analytic solution of Eq. (B5). The plus and minus signs indicate the sign of the buoyancy forcing function $[-\partial(\rho_0 B)/\partial z]$ (where B is buoyancy and ρ_0 is the base-state density) along the top and bottom of the parcel (adapted from Fig. 16-3 of Feynmann et al. 1964).

For convenience, we define $p^* = p_B^* + p_D^*$, the pressure perturbation in terms of two partial pressures resulting from the buoyancy force and the dynamic force, respectively. From this definition it follows that $F_B = \nabla^2 p_B^*$ and $F_D = \nabla^2 p_D^*$.

The term F_D is small at cumulus scales in nontornadic storms as is the case in the Florida storms under investigation. Thus, Eq. (B4) reduces to

$$\nabla^2 p_B^* = F_B = \frac{\partial}{\partial z}(\rho_0 B), \qquad (B5)$$

which is similar in form to Poisson's equation in electrostatics, $\nabla \cdot (\nabla \Phi) = -4\pi\rho$, where Φ is the electrostatic potential and $4\pi\rho$ is the charge density. Thus p_B^* plays the part of the electrostatic potential and $-F_B$ plays the part of charge density. The electric field E is equal to the negative gradient of electrostatic potential ($E = -\nabla\Phi$), thus ensuring that positive charges move downgradient from higher to lower potential. Similarly, the buoyancy pressure gradient acceleration (BPGA) field is defined as $-\rho_0^{-1}\nabla p_B^*$ such that a pressure gradient forces air from high to low pressure. For simple spatial arrangements of buoyancy (charge), we can use mathematical solutions to Poisson's equation to find the vector field of BPGA (electric field).

The force field of BPGA is shown in Fig. B1 for a uniformly buoyant parcel of finite dimensions. It is obtained analytically as the solution of (B5). The plus and minus signs in the figure indicate the sign of $-F_B$ along the top and bottom of the parcel. Where $-F_B > 0$ the BPGA field diverges, and where $-F_B < 0$ it converges, everywhere except along the top and bottom of the parcel $-F_B = 0$. The force field lines of the BPGA field are exactly the same as lines of electric field for finite horizontal plates of opposite charge density. These are lines of force on the air; they do not necessarily indicate the movement of the air itself.

Within the parcel, the lines of BPGA field are downward. The pressure gradient force is downward within the parcel and acts to slow the upward acceleration of the parcel. There is divergence of the BPGA field at the top of the parcel and convergence at the bottom. Outside the parcel, lines of force are up above the parcel, downward in the regions to the sides of the parcel, and upward just below the parcel. These lines indicate directions of forces acting to produce compensating motions in the environment that are required to satisfy mass continuity when the buoyant parcel moves upward. The downward lines of force on the sides of the parcel imply that the upward acceleration of the buoyant parcel is counteracted to some degree by a downward BPGA. This counteraction must occur because some of the buoyancy of the parcel has to be used to move environmental air out of the way in order to preserve mass continuity while the parcel rises. The only way for the downward BPGA to be absent would be to have the parcel width shrink to zero—a nonsensical

case, but nonetheless illustrative of the fact that a given amount of buoyancy produces a larger upward acceleration the narrower the parcel. The scale of buoyant elements resolved by radar data in this investigation is a few kilometers in width. Model results have shown that in cumulus and cumulonimbus clouds, the distribution of B is such that the BPGA is often the same order of magnitude as B (Ferrier and Houze 1989). Thus, the net acceleration experienced by the parcel is the result of the buoyancy of the parcel (upward), the pressure gradient acceleration within the parcel itself (downward), and the pressure gradient acceleration outside the parcel (downward) of air being pushed out of the way as a result of mass continuity.

The upper-level downdrafts are a result of the BPGA field. At the top of the parcel, ambient air is being pushed out of the way of the parcel. This horizontally moving air creates horizontal convergence between the rising parcel and its environment. It is this localized convergence that is associated with the forcing of upper-level downdrafts.

APPENDIX C

Differential Reflectivity: Guidelines for Interpretation

Calculations of differential reflectivity for uniformly distributed particles yield some guidelines for interpreting Z_{DR} values in nature (Herzegh and Jameson 1992). Horizontally oblate particles such as raindrops are characterized by $Z_{HH} > Z_{VV}$, yielding positive Z_{DR} values of 0.5–5 dB. Spherical particles have $Z_{HH} \sim Z_{VV}$ and Z_{DR} values within ± 0.5 dB of zero. Negative Z_{DR} values can be produced by vertically oriented particles, where $Z_{HH} < Z_{VV}$. Graupel and hail can fall in a vertically elongated mode under some conditions and can exhibit negative Z_{DR} values (Hall et al. 1984; Straka and Zrnić 1993). Negative Z_{DR} values are therefore most likely to be formed in regions of strong convective drafts. Vertically elongated raindrops have been found by Takahashi and Kuhara (1993) but are probably rare.

The Gans (1912) scattering theory for oblate and prolate spheroids and assumptions about the equilibrium shapes of drops (Seliga and Bringi 1976; Beard and Chuang 1987) can be used to obtain a relation between Z_{DR} and D_0, the mean diameter of an equivalent volume sphere, for a uniform distribution of raindrops. According to this theory, $Z_{DR} = 1$ corresponds to $D_0 = 2.3$ mm, $Z_{DR} = 2$ dB to 3.6 mm, and $Z_{DR} = 3$ dB to 4.6 mm (Herzegh and Jameson 1992).

A relation between Z_{DR} and diameter for ice particles remains elusive because of the complex scattering properties of ice crystals. Additionally, the refractive index properties of ice make distinguishing between different shapes of ice crystals difficult since the radar return from ice is weak compared to water, independent of particle orientation. The index of refraction is proportional to the bulk density of ice (Battan 1973). The

manner in which the index of refraction term is incorporated into Z_{HH} and Z_{VV} does not lead to its cancellation in the Z_{DR} ratio (Seliga and Bringi 1976). Instead, as the density and index of refraction of the particle decreases, reflectivity becomes weaker and less sensitive to shape and Z_{DR} approaches zero.

Bader et al. (1987), in a high-resolution spatial and temporal comparison between Z_{DR} measurements and in situ aircraft particle measurements, concluded that a few large aggregates of low bulk density, and thus low Z_{DR}, can mask out more numerous needle and column crystals. Ice particle populations above the melting layer in stratiform precipitation regions of mesoscale convective systems have been found by aircraft sampling to be dominated by aggregates (Churchill and Houze 1984; Houze and Churchill 1984, 1987). The shapes of large ice particles, such as horizontally oriented plates and aggregates, are best distinguished by Z_{DR} when they begin to melt.

When an ice particle begins to melt, it becomes coated by a thin film of water, which gives it the refractive index properties of water but approximately the volume and shape of the original ice particle. When the particle melts completely, its volume collapses and its effective diameter and corresponding Z_{DR} are reduced. Differential reflectivity is often used to pinpoint the location of the melting layer on account of its ability to distinguish between precipitation-size ice, melting ice, and liquid water particles (Hall et al. 1984).

REFERENCES

Austin, P. M., S. G. Geotis, J. B. Cunning, J. L. Thomas, R. I. Sax, and J. R. Gillespie, 1976: Raindrop size distributions and $Z-R$ relationships for GATE. Paper, *10th Tech. Conf. Hurricanes and Tropical Meteorology.* [Abstract published in *Bull. Amer. Meteor. Soc.,* **57**, p. 518.]

Bader, M. J., S. A. Clough, and G. P. Fox, 1987: Aircraft and dual polarization radar observations of hydrometeors in light stratiform precipitation. *Quart. J. Roy. Meteor. Soc.,* **113**, 491–515.

Battan, L. J., 1973: *Radar Observation of the Atmosphere.* The University of Chicago Press, 324 pp.

Beard, K. V., and C. Chuang, 1987: A new model for the equilibrium shape of raindrops. *J. Atmos. Sci.,* **44**, 1509–1524.

Biggerstaff, M. I., and R. A. Houze Jr., 1991: Kinematic and precipitation structure of the 10–11 June 1985 squall line. *Mon. Wea. Rev.,* **119**, 3035–3065.

——, and ——, 1993: Kinematics and microphysics of the transition zone of a midlatitude squall-line system. *J. Atmos. Sci.,* **50**, 3091–3110.

Black, M. L., R. W. Burpee, and F. D. Marks Jr., 1991: Vertical motions in tropical cyclones determined with airborne Doppler radial velocities. Preprints, *19th Conf. on Hurricanes and Tropical Meteorology,* Miami, FL, Amer. Meteor. Soc., 409–411.

Braun, S. A., and R. A. Houze Jr., 1994: The transition zone and secondary maximum of radar reflectivity behind a midlatitude squall line: Results retrieved from dual-Doppler data. *J. Atmos. Sci.,* **51**, 2733–2755.

Bringi, V. N., I. J. Caylor, J. Turk, and L. Liu, 1993: Microphysical and electrical evolution of a convective storm using multiparameter radar and aircraft data during CaPE. Preprints, *26th Conf. on Radar Meteor.,* Norman, OK, Amer. Meteor. Soc., 312–314.

Churchill, D. D., and R. A. Houze Jr., 1984: Development and structure of winter monsoon cloud clusters on 10 December 1978. *J. Atmos. Sci.,* **41**, 933–960.

Cunning, J. B., 1986: The Oklahoma–Kansas Preliminary Regional Experiment for STORM-Central. *Bull. Amer. Meteor. Soc.,* **67**, 1478–1486.

Detweiler, A. G., and P. L. Smith, 1992: T-28 participation in the Convection and Precipitation/Electrification (CaPE) Experiment. Report SDSMT/IAS/R-92/04, Institute of Atmospheric Sciences, South Dakota School of Mines and Technology, Rapid City, SD, 76 pp.

Dodge, J., J. Arnold, G. Wilson, J. Evans, and T. T. Fujita, 1986: The Cooperative Huntsville Meteorological Experiment (COHMEX). *Bull. Amer. Meteor. Soc.,* **67**, 417–419.

Donaldson, R. J., Jr., 1961: Radar reflectivity profiles in thunderstorms. *J. Meteor.,* **18**, 292–305.

Emanuel, K. A., 1981: A similarity theory for unsaturated downdrafts within clouds. *J. Atmos. Sci.,* **38**, 1541–1557.

Ferrier, B. S., and R. A. Houze Jr., 1989: One-dimensional time-dependent modeling of GATE cumulonimbus convection. *J. Atmos. Sci.,* **46**, 330–352.

Feynman, R. P., R. B. Leighton, and M. Sands, 1964: *The Feynmann Lectures on Physics, Volume II.* Addison-Wesley, 538 pp.

Fulton, R., and G. M. Heymsfield, 1991: Microphysical and radiative characteristics of convective clouds during COHMEX. *J. Appl. Meteor.,* **30**, 98–116.

Gamache, J. F., and R. A. Houze Jr., 1982: Mesoscale air motions associated with a tropical squall line. *Mon. Wea. Rev.,* **110**, 118–135.

——, and ——, 1985: Further analysis of the composite wind and thermodynamic structure of the 12 September GATE squall line. *Mon. Wea. Rev.,* **113**, 1241–1259.

Gans, R., 1912: Über die Form ultramikroskopischer Goldteilchen. *Ann. Phys.,* **37**, 881–900.

Hall, M. P. M., S. M. Cherry, J. W. F. Goddard, and G. R. Kennedy, 1980: Raindrop sizes and rainrate measured by dual-polarisation radar. *Nature,* **285**, 195–198.

——, J. W. F. Goddard, and S. M. Cherry, 1984: Identification of hydrometeors and other targets by dual-polarization radar. *Radio Sci.,* **19**, 132–140.

Hallett, J., R. I. Sax, D. Lamb, and A. S. Ramachandramurty, 1978: Aircraft measurements of ice in Florida cumuli. *Quart. J. Roy. Meteor. Soc.,* **104**, 631–651.

Herzegh, P. H., and A. R. Jameson, 1992: Observing precipitation through dual-polarization radar measurements. *Bull. Amer. Meteor. Soc.,* **73**, 1365–1374.

Heymsfield, G. M., and S. Schotz, 1985: Structure and evolution of a severe squall line over Oklahoma. *Mon. Wea. Rev.,* **113**, 1563–1589.

Hobbs, P. V., 1974: *Ice Physics.* Oxford Press, 837 pp.

——, S. Chang, and J. D. Locatelli, 1974: The dimensions and aggregation of ice crystals in natural clouds. *J. Geophys. Res.,* **79**, 2199–2206.

Houze, R. A., Jr., 1977: Structure and dynamics of a tropical squall-line system. *Mon. Wea. Rev.,* **105**, 1540–1567.

——, 1989: Observed structure of mesoscale convective systems and implications for large-scale heating. *Quart. J. Roy. Meteor. Soc.,* **115**, 425–461.

——, 1993: *Cloud Dynamics.* Academic Press, 573 pp.

——, and A. K. Betts, 1981: Convection in GATE. *Rev. Geophys. Space Phys.,* **19**, 541–576.

——, and D. D. Churchill, 1984: Microphysical structure of winter monsoon cloud clusters. *J. Atmos. Sci.,* **41**, 3405–3411.

——, and E. N. Rappaport, 1984: Air motions and precipitation structure of an early summer squall line over the eastern tropical Atlantic. *J. Atmos. Sci.,* **41**, 553–574.

——, and D. D. Churchill, 1987: Mesoscale organization and cloud microphysics in a Bay of Bengal depression. *J. Atmos. Sci.,* **44**, 1845–1867.

Hudlow, M. D., 1979: Mean rainfall patterns for the three phases of GATE. *J. Appl. Meteor.,* **18**, 1656–1669.

Illingworth, A. J., J. W. F. Goddard, and S. M. Cherry, 1987: Polarization radar studies in precipitation development in convective storms. *Quart. J. Roy. Meteor. Soc.,* **113**, 469–489.

Jorgensen, D. P., and M. A. LeMone, 1989: Vertical velocity characteristics of oceanic convection. *J. Atmos. Sci.,* **46,** 621–640.

Kingsmill, D. E., and R. M. Wakimoto, 1991: Kinematic, dynamic, and thermodynamic analysis of a weakly sheared severe thunderstorm over northern Alabama. *Mon. Wea. Rev.,* **119,** 262–297.

Knupp, K. R., 1987: Downdrafts within High Plains cumulonimbi. Part I: General kinematic structure. *J. Atmos. Sci.,* **44,** 987–1008.

Konrad, T. G., 1978: Statistical models of summer rainshowers derived from fine-scale radar observations. *J. Appl. Meteor.,* **17,** 171–188.

Leary, C. A., and E. N. Rappaport, 1987: The life cycle and internal structure of a mesoscale convective complex. *Mon. Wea. Rev.,* **115,** 1503–1527.

Locatelli, J. D., and P. V. Hobbs, 1974: Fall speeds and masses of solid precipitation particles. *J. Geophys. Res.,* **79,** 2185–2197.

Mapes, B. E., and R. A. Houze Jr., 1993: An integrated view of the 1987 Australian monsoon and its mesoscale convective systems. Part II: Vertical structure. *Quart. J. Roy. Meteor. Soc.,* **119,** 733–754.

Marks, F. D., Jr., and R. A. Houze Jr., 1987: Inner-core structure of Hurricane Alicia from airborne Doppler-radar observations. *J. Atmos. Sci.,* **44,** 1296–1317.

Mohr, C. G., and L. J. Miller, 1983: CEDRIC—A software package for Cartesian space editing, synthesis and display of radar fields under interactive control. Preprints, *21st Conf. on Radar Meteor.,* Edmonton, Canada, Amer. Meteor. Soc., 559–574.

Oye, R., and R. E. Carbone, 1981: Interactive Doppler editing software. Preprints, *20th Conf. on Radar Meteor.,* Boston, MA, Amer. Meteor. Soc., 683–689.

Paluch, I. R., 1979: The entrainment mechanism in Colorado cumuli. *J. Atmos. Sci.,* **36,** 2467–2478.

Pruppacher, H. R., and J. D. Klett, 1978: *Microphysics of Clouds and Precipitation.* D. Reidel, 714 pp.

Raymond, D. J., R. Solomon, and A. M. Blyth, 1991: Mass fluxes in New Mexico mountain thunderstorms from radar and aircraft measurements. *Quart. J. Roy. Meteor. Soc.,* **117,** 587–621.

Rinehart, R. E., 1991: *Radar for Meteorologists.* 2d ed. University of North Dakota, 334 pp.

Rogers, R. R., and M. K. Yau, 1989: *A Short Course in Cloud Physics.* 3d ed. Pergamon Press, 293 pp.

Rotunno, R., and J. B. Klemp, 1982: The influence of shear-induced pressure gradient on thunderstorm motion. *Mon. Wea. Rev.,* **110,** 136–151.

Rutledge, S. A., R. A. Houze Jr., M. I. Biggerstaff, and T. Matejka, 1988: The Oklahoma–Kansas mesoscale convective system of 10–11 June 1985: Precipitation structure and single Doppler radar analysis. *Mon. Wea. Rev.,* **116,** 1409–1430.

Seliga, T. A., and V. N. Bringi, 1976: Potential use of radar differential reflectivity measurements at orthogonal polarizations for measuring precipitation. *J. Appl. Meteor.,* **15,** 69–76.

——, and K. Aydin, 1983: Possible detection of widespread glaciation throughout upper regions of a storm after local sunset from differential reflectivity (ZDR) measurements during CCOPE. Preprints, *21th Conf. on Radar Meteorology,* Edmonton, Canada, Amer. Meteor. Soc., 503–507.

——, J. L. Peterson, and V. N. Bringi, 1981: Hydrometeor characteristics in the May 2, 1979 squall line in central Oklahoma as obtained from radar differential reflectivity measurements during SESAME. Preprints, *20th Conf. on Radar Meteorology,* Boston, MA, Amer. Meteor. Soc., 561–566.

Simpson, J., R. F. Adler, and G. R. North, 1988: A proposed Tropical Rainfall Measuring Mission (TRMM) satellite. *Bull. Amer. Meteor. Soc.,* **69,** 278–295.

Smull, B. F., and R. A. Houze Jr., 1987a: Dual-Doppler radar analysis of a midlatitude squall line with a trailing region of stratiform rain. *J. Atmos. Sci.,* **44,** 2128–2148.

——, and ——, 1987b: Rear inflow in squall lines with trailing stratiform precipitation. *Mon. Wea. Rev.,* **115,** 2869–2889.

——, and J. A. Augustine, 1993: Multiscale analysis of a mature mesoscale convective complex. *Mon. Wea. Rev.,* **121,** 103–132.

Squires, P., 1958: Penetrative downdraughts in cumuli. *Tellus,* **10,** 381–389.

Srivastava, R. C., 1985: A simple model of evaporatively driven downdraft application to microburst downdraft. *J. Atmos. Sci.,* **42,** 1004–1023.

——, 1987: A model of intense downdrafts driven by the melting and evaporation of precipitation. *J. Atmos. Sci.,* **44,** 1752–1773.

——, T. J. Matejka, and T. J. Lorello, 1986: Doppler-radar study of the trailing anvil region associated with a squall line. *J. Atmos. Sci.,* **43,** 356–377.

Straka, J. M., and D. S. Zrnić, 1993: An algorithm to deduce hydrometeor types and content from multi-parameter radar data. Preprints, *26th Conf. on Radar Meteorology,* Norman, OK, Amer. Meteor. Soc., 513–515.

Szoke, E. J., E. J. Zipser, and D. P. Jorgensen, 1986: A radar study of convective cells in mesoscale systems in GATE. Part I: Vertical profile statistics and comparisons with hurricanes. *J. Atmos. Sci.,* **43,** 182–197.

Takahashi, T., and K. Kuhara, 1993: Precipitation mechanisms of cumulonimbus clouds at Pohnpei, Micronesia. *J. Meteor. Soc. Japan,* **71,** 21–31.

Tuttle, J. D., V. N. Bringi, H. D. Orville, and F. J. Kopp, 1989: Multiparameter radar study of a microburst: Comparison with model results. *J. Atmos. Sci.,* **46,** 601–620.

Wilson, J. W., and D. Reum, 1988: The flare echo: Reflectivity and velocity signature. *J. Atmos. Oceanic Technol.,* **5,** 197–205.

Yuter, S. E., and R. A. Houze Jr., 1995a: Three-dimensional kinematic and microphysical evolution of Florida cumulonimbus. Part I: Spatial distribution of updrafts, downdrafts and precipitation. *Mon. Wea. Rev.,* **123,** 1921–1940.

——, and ——, 1995b: Three-dimensional kinematic and microphysical evolution of Florida cumulonimbus. Part III: Vertical mass transport, mass divergence and synthesis. *Mon. Wea. Rev.,* **123,** 1964–1983.

Zipser, E. J., 1969: The role of organized unsaturated convective downdrafts in the structure and rapid decay of an equatorial disturbance. *J. Appl. Meteor.,* **8,** 799–814.

——, 1977: Mesoscale and convective-scale downdrafts as distinct components of squall-line circulation. *Mon. Wea. Rev.,* **105,** 1568–1589.

——, and K. R. Lutz, 1994: The vertical profile of radar reflectivity of convective cells: a strong indicator of storm intensity and lightning probability? *Mon. Wea. Rev.,* **122,** 1751–1759.